Laminar flow-induced vibration of a three-degree-of-freedom circular cylinder with an attached splitter plate

Mingjie Zhang (张明杰)[1,a)], Ole Øiseth[1], Fuyou Xu (许福友)[2,a)]

[1]*Department of Structural Engineering, Norwegian University of Science and Technology, 7491, Trondheim, Norway.*

[2]*School of Civil Engineering, Dalian University of Technology, 11602, Dalian, China.*

Authors to whom correspondence should be addressed: mingjie.zhang@ntnu.no and fuyouxu@dlut.edu.cn

Abstract

Splitter plates are widely used for drag reduction and vibration control or enhancement of circular cylinders. The effects of a splitter plate on the vertical flow-induced vibrations of a circular cylinder have been well studied. However, its effects on the vertical-torsional coupled vibrations require further investigation. In this paper, the three-degree-of-freedom (TDoF) flow-induced vibrations of a circular cylinder with an attached splitter plate are numerically investigated at a Reynolds number of 100. The ratio between the torsional and vertical natural frequencies is varied within $f_{\theta,0}/f_{h,0}$ = 6, 4, 3, 2, and 1. Numerical results show that the flow-induced vibrations of a TDoF cylinder-plate assembly, depending on the frequency ratio, may differ significantly from those of a single-degree-of-freedom (SDoF) vertical or torsional assembly. For cylinder-plate assemblies with $f_{\theta,0}/f_{h,0}$ = 6 ~ 2, the vibrations can be divided into a vertical vibration-dominated branch (V branch), a torsional vibration-dominated branch (T branch), and a coupled vibration-dominated branch (C branch). The V branch vibration of a TDoF assembly is similar to that of an SDoF vertical assembly at the same reduced flow velocity, while the difference increases with decreasing the frequency ratio. The T branch vibration of a TDoF assembly is almost identical to the vibration of an SDoF torsional assembly at the same reduced flow velocity. The ratio between the torsional and vertical vibration amplitudes increases with decreasing the frequency ratio in the C branch. For the assembly with $f_{\theta,0}/f_{h,0}$ = 1, vertical-torsional coupled VIVs are observed with the largest torsional amplitude as high as 46.3°. The vibrations of TDoF assemblies with all considered frequency ratios may be more severe than those of SDoF vertical and torsional assemblies within specific ranges of reduced flow velocities. The mean drag coefficients for the $f_{\theta,0}/f_{h,0}$ = 6 ~ 2 assemblies are lower than a stationary circular cylinder but often higher than a stationary cylinder-plate assembly. The mean drag coefficients for the $f_{\theta,0}/f_{h,0}$ = 1 assembly in the lock-in range are considerably larger than that of a stationary circular cylinder. For TDoF assemblies with $f_{\theta,0}/f_{h,0}$ = 6 ~ 2, the V branch and C branch vibrations are mainly driven by the interaction between the assembly and the shear layers, while the T branch vibrations are excited by the typical 2S mode of vortex shedding. The 2S vortex shedding mode is also observed in the lock-in range of the $f_{\theta,0}/f_{h,0}$ = 1 assembly.

Keywords: Circular cylinder; Splitter plate; Flow-induced vibration; Natural frequency ratio.

I. Introduction

Flow-induced vibrations of circular cylinders have been extensively studied as one of the most classical problems in fluid mechanics. These vibrations are undesirable in many engineering fields since they may raise significant concerns about the fatigue life and/or safety of a structure, e.g., marine risers,[1, 2] bridge cables,[3, 4] pipelines,[5, 6] and heat exchanger tubes.[7, 8] More recently, these vibrations have been recognised as a competitive choice for wind and hydro energy harvesting.[9-11] Various active and passive control measures have been designed to mitigate or enlarge the flow-induced vibrations of circular cylinders.[12-19]

A thin rigid plate positioned in the wake of a circular cylinder has been widely investigated as a passive control device. The device was firstly studied by Roshko[20], who showed that a splitter plate can weaken or even inhibit, depending on its length and position, the vortex shedding from a stationary circular cylinder. Bearman[21] showed that a splitter plate substantially increases the base pressure and reduces the drag force of a stationary cylinder. Gerrard [22] experimentally measured the vortex formation length and Strouhal number for a stationary circular cylinder with an attached splitter plate with a length of $L = 0 \sim 2.0D$, where D is the diameter of the circular cylinder. Following these pioneering studies, experimental measurements and numerical simulations in an extensive range of Reynolds numbers confirmed that a splitter plate (attached to or detached from the circular cylinder) can enlarge the base pressure, decrease the drag, narrow the wake width, and influence the Strouhal number.[23-27] For an attached splitter plate, there is a critical plate length beyond which vortex shedding can be completely suppressed and an optimal length at which a minimum drag can be achieved.[23, 24] The effect of a splitter plate also depends on the gap between the circular cylinder and the splitter plate, with the detached splitter plate becomes ineffective once the gap exceeds a critical value.[25, 26]

A splitter plate is also known to influence the flow-induced vibrations of a circular cylinder. Considerable efforts have been advanced to study the effects of a splitter plate on the vertical vibration of a circular cylinder. Kawai[28] experimentally showed that, instead of vortex-induced vibrations (VIVs) for a circular cylinder, galloping-type vibrations occur for a cylinder-plate assembly with a plate length of $L = D \sim 4D$. Nakamura et al.[29] investigated the vertical flow-induced vibrations of a circular cylinder with a detached splitter plate ($L = 31.3D$, $G = 0.1D$, where G is the gap between the cylinder and the plate) through wind tunnel experiments. They showed that the cylinder-plate assembly can gallop while the quasi-steady aerodynamic theory cannot predict the critical wind velocity for galloping instability. Stappenbelt[30] studied the vertical flow-induced vibrations of a low-aspect-ratio circular cylinder with an attached splitter plate through still-water towing experiments. Depending on the splitter plate length, three global response behaviors were observed: VIVs at $L \leq 0.5D$, interfered VIV and galloping vibrations at $L = D \sim 2.4D$, and no significant vibrations at $L = 2.8D \sim 4.0D$. The transition from VIV to galloping with increasing the plate length was confirmed numerically by Sun et al.[31] for a circular cylinder with an attached splitter plate in laminar flow. Liang et al.[32] studied the vertical flow-induced vibrations of a circular cylinder with a detached splitter plate ($L = 0.4D \sim 5.0D$, $G = 0.2D$) through wind tunnel experiments. Different global response behaviours, i.e., VIV, interfered VIV and galloping, and separated VIV and galloping, were also observed with increasing the plate length. More investigations on the vertical flow-induced vibrations of a circular cylinder with an attached or detached splitter plate can be found in several other papers.[33-36]

In addition to vertical galloping, a circular cylinder with a splitter plate may vibrate torsionally due to the flow-induced torsional moment. Cimbala and co-authors[37, 38] reported wind tunnel experiments on a cylinder-plate assembly that is free to rotate around the centre of the circular cylinder, that is, the structural stiffness in the torsional degree of freedom is zero. They found that a cylinder-plate assembly with an $L = 4D$ splitter plate rotates around its original equilibrium position. However, for an assembly with $L \leq 3D$, a symmetry-breaking bifurcation occurred, that is, the equilibrium position migrated to a non-zero angle at either side of its central line. For the same freely rotatable cylinder-plate assembly, Xu et al.[39] studied the migration of equilibrium position numerically and confirmed that the phenomenon can be predicted based on its steady-state flow-induced moment coefficients. More recently, Lu et al.[40] studied the flow-induced vibrations of a cylinder-plate assembly elastically mounted in the torsional degree of freedom. Torsional VIVs were observed at lower reduced flow velocities, while a symmetry-breaking bifurcation occurred as the reduced flow velocity increases, after which the cylinder-plate assembly vibrated around a non-zero equilibrium angle. Based on further numerical simulations, Zhang et al.[41] showed that for an elastically mounted torsional cylinder-plate assembly, the peak VIV amplitude increases, and the critical flow velocity for symmetry-breaking bifurcation reduces with decreasing the moment of inertia.

To the authors' knowledge, all previous studies on flow-induced vibrations of a circular cylinder with a splitter plate considered a single-degree-of-freedom (SDoF) vibration in the vertical or torsional direction, or considered a two-degree-of-freedom vibration in vertical and in-flow directions. For a cylinder-plate assembly elastically mounted in the vertical and in-flow directions, the response is often dominated by the vertical vibration while the in-flow vibration is insignificant.[31] However, for a cylinder-plate assembly elastically mounted in the vertical, in-flow, and torsional directions, the vibration response remains unknown and hence requires further investigation.

Thus, this paper studies numerically the flow-induced vibrations of a cylinder-plate assembly elastically mounted in the vertical, in-flow, and torsional directions. The splitter plate length L equals the cylinder diameter D. The critical Reynolds number of this configuration for the onset of vortex shedding is round $Re = \rho UD/\mu = 48$,[39] where ρ is the fluid mass density, U is the flow velocity, μ is the fluid dynamic viscosity. The vertical and in-flow natural frequencies are the same, while various ratios between the torsional and vertical frequencies are considered. It is shown that the flow-induced vibrations of a three-degree-of-freedom (TDoF) cylinder-plate assembly, depending on the frequency ratio, may differ from those of the SDoF vertical and torsional assemblies. If the torsional frequency is higher than two times the vertical frequency, the vibrations can be divided into three branches in which the responses of different degrees of freedom are dominant. Vertical-torsional coupled VIVs are observed if the torsional frequency equals the vertical frequency. The flow-induced forces and the wake patterns during the vibrations are also discussed.

The remainder of this paper is organised as follows. Section II describes the configuration of the considered cylinder-plate assembly, the computational domain, and the mesh arrangement. Section III introduces the governing equations of the fluid-structure interaction system and provides a validation of the developed numerical model. Section IV presents and discusses the simulation results. Section V summarises the main conclusions.

II. Structure configuration, computational domain, and mesh arrangement

The considered structure is a circular cylinder (diameter = D) with a rigid splitter plate (length $L = D$, thickness = $0.02D$) connected to its rear stagnation point, as presented in Fig. 1. This specific configuration is selected because its SDoF vertical or torsional vibrations have been well investigated in previous papers.[31, 41] The cylinder-plate assembly is subjected to a uniform flow with a constant velocity U. The assembly is elastically mounted in the vertical, in-line, and torsional degrees of freedom. The stiffness centre is located at the centre of the circular cylinder for all degrees of freedom.

Fig. 1 shows the computational domain and boundary conditions, which are the same as the authors' previous paper.[41] The two-dimensional computational domain includes a rigid region that moves together with the structure, a dynamic region that accommodates the displacement of the inner rigid region, and a static region that remains static during the simulation process. The computational domain is $50D \times 100D$ in size, resulting in a blockage ratio of 2%.

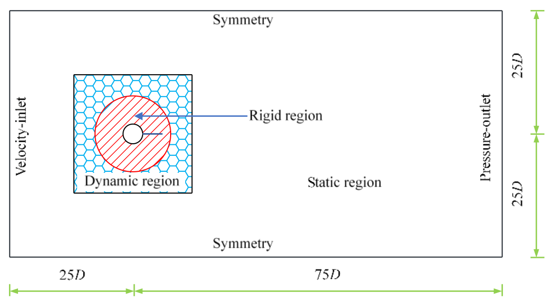

FIG. 1. Model configuration, computational domain, and boundary conditions.

The mesh arrangement of the present paper is similar to that described in Zhang et al.[41] Structured grids are used in the whole computational domain and the total grid number is 76,990. The surface of the circular cylinder is distributed evenly into 276 grid cells, and each side of the splitter plate is distributed evenly into 94 grid cells. A mesh dependency test was conducted before the simulations, which followed the same procedure and utilised three meshes of different grid densities described in Zhang et al.[41] The test confirmed that the present mesh is refined enough to obtain converged numerical solutions.

III. Governing equations, numerical methodology, and code validation

The equations of motion of the cylinder-plate assembly can be expressed as

$$m\left(\ddot{h} + 4\pi f_{h,0}\xi_{h,0}\dot{h} + 4\pi^2 f_{h,0}^2 h\right) = F_L, \tag{1}$$

$$m\left(\ddot{p} + 4\pi f_{p,0}\xi_{p,0}\dot{p} + 4\pi^2 f_{p,0}^2 p\right) = F_D, \tag{2}$$

$$I\left(\ddot{\theta} + 4\pi f_{\theta,0}\xi_{\theta,0}\dot{\theta} + 4\pi^2 f_{\theta,0}^2 \theta\right) = F_M, \tag{3}$$

where m and I are the mass and moment of inertia per unit length, respectively; h, p, and θ are the vertical, in-line, and torsional displacements, respectively; the overdot represents the derivative with respect to time t; $f_{h,\,0}$, $f_{p,\,0}$, $f_{\theta,\,0}$ are the vertical, in-line, and torsional natural frequencies, respectively; $\xi_{h,\,0}$, $\xi_{p,\,0}$, $\xi_{\theta,\,0}$ are the vertical, in-line, and torsional structural damping ratios, respectively. F_L, F_D, and F_M are fluid-induced lift, drag, and torsional moment per unit length, respectively.

If the circular cylinder is a pipe with the same material and thickness as the splitter plate, i.e., $0.02D$, the equations of motion can be expressed in a dimensionless form as

$$H'' + \frac{4\pi\xi_{h,0}}{U_{r,h}}H' + \left(\frac{2\pi}{U_{r,h}}\right)^2 H = \frac{50}{25\pi+2}\frac{C_L}{m^*}, \tag{4}$$

$$P'' + \frac{4\pi\xi_{p,0}}{U_{r,p}}P' + \left(\frac{2\pi}{U_{r,p}}\right)^2 P = \frac{50}{25\pi+2}\frac{C_D}{m^*}, \quad (5)$$

$$\theta'' + \frac{4\pi\xi_{\theta,0}}{U_{r,\theta}}\theta' + \left(\frac{2\pi}{U_{r,\theta}}\right)^2 \theta = \frac{50}{25\pi+2}\frac{\bar{F}_M}{m^*}, \quad (6)$$

where $H = h/D$ and $P = p/D$ are the dimensionless vertical and in-line displacements, respectively; the the prime represents the derivative with respect to the dimensionless time $\tau = Ut/D$; $U_{r,i} = U/(f_{i,0}d)$ ($i = h$, p, or θ) represents the reduced flow velocity; in the following parts, $U_{r,h}$ and $U_{r,\theta}$ will be referred to as the vertical and torsional reduced flow velocities, respectively; C_L and C_D are dimensionless lift coefficient and drag coefficient normalised by $0.5\rho U^2 D$, respectively; $\bar{F}_M$ is the dimensionless fluid-induced torsional moment; m^* is the mass ratio between the cylinder-plate assembly and the displaced fluid.

$$\bar{F}_M = \frac{F_M}{\rho I U^2/(2m_s)}, \quad (7)$$

$$m^* = \frac{m}{\pi\rho D^2/4 + \rho D^2/50}. \quad (8)$$

The governing equations of the fluid are written in an arbitrary Lagrangian-Eulerian formulation and solved by the finite volume method. The flow field is solved in the commercial platform ANSYS Fluent. The first-order implicit time integration scheme is adopted for temporal discretisation. The second-order upwind and least square cell-based schemes are employed for spatial discretisations of the convection and diffusion terms, respectively. The semi-implicit method for the pressure-linked equations (SIMPLE) algorithm is utilised to solve the pressure-velocity coupled algebraic equations. The equations of motion of the cylinder-plate assembly are integrated by using the 4$^{\text{th}}$-order Runge-Kutta method. The fluid-structure interaction is achieved following the loosely coupled partitioned approach. The solver has been proven accurate and stable in simulating the flows past and the flow-induced vibrations of various bluff bodies, e.g., circular cylinders, rectangular cylinders, and bridge decks.[41-44] As an example, Fig. 2 compares the simulated vertical vibration amplitudes $h_{\max}$ and vibration frequencies f_h of the cylinder-plate assembly in Fig. 1 with the numerical results of Sun et al.[31] Both simulations were conducted at $m^* = \frac{m_s}{(\pi\rho D^2/4+\rho D^2/50)} = 10$ and $\xi_{h,0} = 0$. The Reynolds number is $Re = 100$. The in-line and torsional degrees of freedom were not considered. It is noted that the present numerical results agree well with the previous results[31] in terms of both vibration amplitude and vibration frequency.

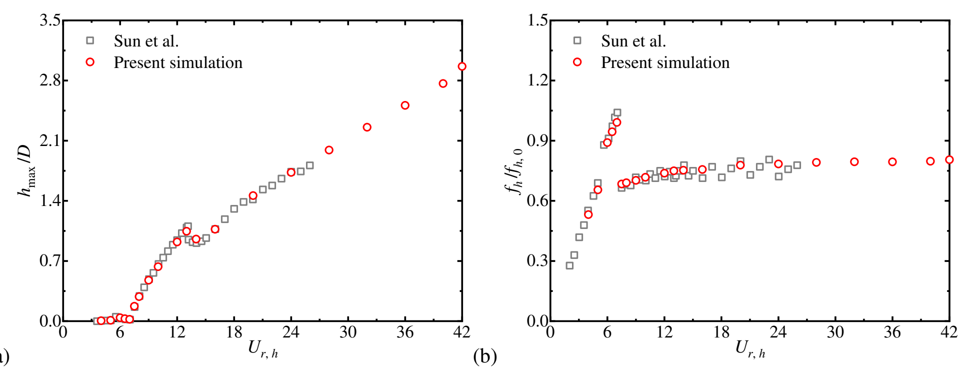

(a) (b)

FIG. 2. Comparison between present results and the results of Sun et al.[31]: (a) vertical vibration amplitude and (b) vertical vibration frequency.

IV. Numerical results and discussions

For a circular-cylinder assembly elastically mounted in the vertical, in-line, and torsional degrees of freedom, the flow-induced vibrations within a reduced flow velocity range of $U_{r,h}$ = 2 to 42 are simulated using the numerical procedure described in Sections II and III. The vertical and in-line natural frequencies are the same, i.e., $f_{h,0} = f_{p,0}$. Five torsional-to-vertical frequency ratios, i.e., $f_{\theta,0}/f_{h,0}$ = 6, 4, 3, 2, and 1, are considered to investigate the influences of frequency ratio on the flow-induced vibrations. The structural damping ratios are $\xi_{h,0} = \xi_{p,0} = \xi_{\theta,0} = 0$. A two-dimensional and laminar flow with a Reynolds number of Re = 100 remains throughout the simulations. The flow velocity remains constant and the reduced velocity is varied by changing the natural frequency. The circular cylinder is assumed as a pipe with the same thickness as the splitter plate, i.e., $T_p = 0.02D$. Hence, the uniform mass density ρ_s and moment of inertia I of the cylinder-plate assembly can be calculated as

$$\rho_s = \frac{m^{*}\cdot(\pi\rho D^2/4+\rho D^2/50)}{\pi D T_p + D T_p}, \tag{9}$$

$$I = \rho_s \pi D T_p \left(\frac{D}{2}\right)^2 + \rho_s D T_p \frac{13D^2}{12}. \tag{10}$$

It is stated that the flow-induced vibrations of a cylinder-plate assembly depend significantly on the plate length.[31, 34] Hence, more investigations are necessary to study the flow-induced vibrations of TDoF assemblies with different splitter plate lengths.

A. Vibration amplitude, vibration frequency, and displacement signal

Fig. 3 presents the steady-state vertical vibration amplitudes h_{max} and torsional vibration amplitudes θ_{max} of cylinder-plate assemblies with various frequency ratios. The in-line vibrations are insignificant and hence not analysed in this paper. The results for an assembly limited to vertical vibration and an assembly limited to torsional vibration are also presented for comparison. In the following parts, the assembly elastically mounted in three degrees of freedom will be referred to as the TDoF (three-degree-of-freedom) assembly; the assembly limited to vertical or torsional vibration will be referred to as the SDoF (single-degree-of-freedom) vertical assembly or SDoF torsional assembly. The shading and arrows in Fig. 3 only apply for the TDoF cases.

It is noted that for the SDoF vertical assembly, remarkable vibrations are observed as the reduced velocity $U_{r,h}$ becomes higher than 7.5 and the vibration amplitude increases continuously with increasing $U_{r,h}$. The SDoF torsional assembly exhibits VIVs within a reduced velocity range of $U_{r,\theta}$ = 5.5 ~ 10. As shown in Fig. 3(a), the response for the $f_{\theta,0}/f_{h,0}$ = 6 assembly is dominated by the vertical vibration while the torsional amplitude is lower than 3° at $U_{r,h} = 6U_{r,\theta} < 30$. In this range of reduced velocities, both the vertical amplitude and the torsional amplitude of the $f_{\theta,0}/f_{h,0}$ = 6 assembly increase continuously with increasing the reduced velocity. The vertical amplitude of the $f_{\theta,0}/f_{h,0}$ = 6 assembly is close to that of the SDoF vertical assembly, while the torsional amplitude is considerably larger than that of the SDoF torsional assembly at the same reduced velocity. At $U_{r,h} = 6U_{r,\theta}$ = 32 ~ 36, the response for the $f_{\theta,0}/f_{h,0}$ = 6 assembly is dominated by the torsional vibration while the vertical vibration amplitude is close to zero. The torsional amplitude of the $f_{\theta,0}/f_{h,0}$ = 6 assembly is slightly larger than that of the SDoF torsional assembly at the same reduced velocity. The vibrations of the $f_{\theta,0}/f_{h,0}$ = 6 assembly may be more dangerous than those of SDoF assemblies at certain reduced velocities. More specifically, the vibration of the TDoF assembly may be more dangerous than that of the SDoF vertical assembly for $U_{r,h} < 30$ due to the coupled torsional motion (the vertical vibration amplitudes are close). In addition, the vibration of the TDoF assembly is more dangerous than that of the SDoF torsional assembly for $U_{r,h}$ < 32 ~ 36 due to the increased vibration amplitude. The torsional amplitude of the $f_{\theta,0}/f_{h,0}$ = 6 assembly decreases continuously with increasing the reduced velocity while the vertical amplitude exhibits a sharp jump at around $U_{r,h} = 6U_{r,\theta} = 38$. After this sharp jump, the $f_{\theta,0}/f_{h,0}$ = 6 assembly exhibits vertical-torsional coupled vibrations with significant vibration amplitudes in both degrees of freedom.

Some unified observations for the vibrations of TDoF assemblies with $f_{\theta,0}/f_{h,0}$ = 6, 4, 3, and 2 can be noticed from Figs. 3(a) ~ 3(d). The vibrations of TDoF assemblies are dominated by vertical vibrations at lower reduced velocities before the lock-in range for torsional VIVs. However, within the lock-in range for torsional VIVs, the vibrations of TDoF assemblies are dominated by torsional vibrations. At higher reduced velocities beyond this lock-in range, the TDoF assemblies exhibit vertical-torsional coupled vibrations with significant vibration amplitudes in both degrees of freedom. Hence, the vibrations of a TDoF assembly with $f_{\theta,0}/f_{h,0}$ = 2 ~ 6 can be divided into three branches, i.e., a vertical vibration-dominated branch (V branch), a torsional vibration-dominated branch (T branch), and a coupled vibration-dominated branch (C branch). The V branch starts at around $U_{r,h}$ = 7.5 and terminates at around $U_{r,\theta}$ = 5.0, the T branch occurs at around $U_{r,\theta}$ = 5.0 ~ 6.0, and the C branch occurs at higher $U_{r,\theta}$ values. With decreasing the frequency ratio, the T branch moves to a range with lower $U_{r,h}$ values, while the $U_{r,h}$ ranges for the V branch and the C branch shrinks and extends, respectively. In the V branch, the vertical vibration amplitude of the TDoF assembly is lower than that of the SDoF vertical assembly, and the difference increases with decreasing the frequency ratio. Considerable torsional vibration exists in the V brach, and the torsional vibration amplitude increases with decreasing the frequency ratio. The vibration in the T branch is close to an SDoF torsional vibration, with an amplitude slightly higher than the value of an SDoF torsional assembly. The vibration amplitude in the torsional branch is insignificantly affected by the frequency ratio. The vibration in the C branch is a vertical-torsional coupled vibration with significant vibration amplitudes in both degrees of freedom. The ratio between the torsional and vertical amplitudes increases with decreasing the frequency ratio.

As seen from Fig. 3(e), the global response behavior of the TDoF assembly with $f_{\theta,0}/f_{h,0}$ = 1 is significantly different from those of TDoF assemblies with $f_{\theta,0}/f_{h,0}$ = 6, 4, 3, and 2. The $f_{\theta,0}/f_{h,0}$ = 1 assembly exhibits VIVs in a lock-in range of $U_{r,h} = U_{r,\theta}$ = 5.0 ~ 13.0. Significant torsional vibrations are observed. The largest torsional amplitude in the lock-in range is as high as 46.3°. The vertical vibration amplitudes of the $f_{\theta,0}/f_{h,0}$ = 1 assembly in the lock-in range are also higher than the SDoF vertical assembly, with some exceptions at the end of the lock-in range. No significant vibrations exist for the $f_{\theta,0}/f_{h,0}$ = 1 assembly outside the lock-in range. Similar to the SDoF torsional assembly[40], a symmetry-breaking bifurcation occurs as the reduced velocity increases, which will be discussed later in this Section.

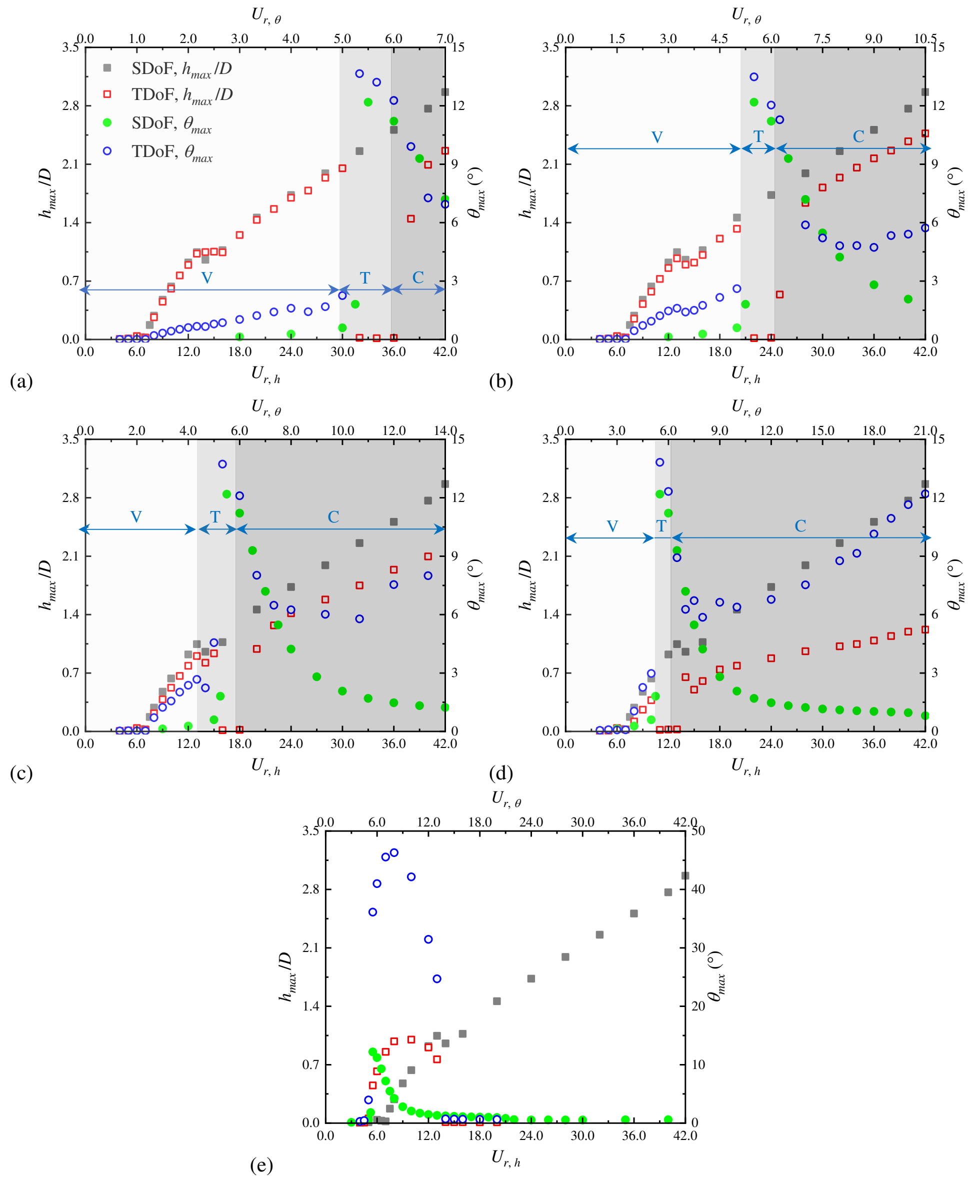

FIG. 3. Steady-state vertical and torsional vibration amplitudes of cylinder-plate assemblies with various frequency ratios: (a) $f_{\theta,0}/f_{h,0}$ = 6; (b) $f_{\theta,0}/f_{h,0}$ = 4; (c) $f_{\theta,0}/f_{h,0}$ = 3; (d) $f_{\theta,0}/f_{h,0}$ = 2; (e) $f_{\theta,0}/f_{h,0}$ = 1. The shading and arrows only apply for the TDoF cases.

Fig. 4 shows the steady-state vertical vibration frequencies f_h and the torsional vibration frequencies f_θ of cylinder-plate assemblies with various frequency ratios. The results for the SDoF vertical assembly and the SDoF torsional assembly are also given for comparison. It is noted that the natural frequencies change with the reduced velocity since the flow velocity remains constant in the present simulations. The global frequency response behaviors are similar for assemblies with $f_{\theta,0}/f_{h,0}$ = 6, 4, 3, and 2; hence, the results for $f_{\theta,0}/f_{h,0}$ = 4 and 2 are not shown for brevity. The value given in Fig. 4 represents the dominant frequency for a displacement signal that includes multiple frequencies. The dominant frequency is observed via visual inspection of the FFT spectra. For the SDoF vertical assembly, the vibration frequency f_h is lower than the natural frequency $f_{h,0}$ outside the lock-in range, while f_h approaches $f_{h,0}$ in the lock-in range. For the SDoF torsional assembly, the vibration frequency f_θ is also lower than the natural frequency $f_{\theta,0}$ before the lock-in range. However, f_θ approaches $f_{\theta,0}$ in the lock-in range and becomes larger than $f_{\theta,0}$ after the lock-in range. Detailed analyses of the frequency responses of SDoF vertical and torsional assemblies can be found in[31, 40, 41].

As seen from Figs. 4(a) and 4(b) for TDoF assemblies with $f_{\theta,0}/f_{h,0}$ = 6 and 3, the vertical and torsional vibration frequencies are consistent with some exceptions at two sides of the T branch. In the V branch and the C branch, the vibration frequency of the TDoF assembly follows the same vibration frequency as the SDoF vertical assembly at the same reduced velocity. However, in the T branch, the vibration frequency of the TDoF assembly follows the same vibration frequency as the SDoF torsional assembly. At two sides of the T branch, the vertical and torsional frequencies of the TDoF assembly follow the vibration frequencies of the SDoF vertical and SDoF torsional assemblies, respectively.

For the TDoF assembly with $f_{\theta,0}/f_{h,0}$ = 1 shown in Fig. 4(c), the vertical and torsional vibration frequencies are always consistent. As seen from the left part of Fig. 4(c), the vibration frequencies outside the lock-in range are close to the vortex shedding frequency of a stationary cylinder-plate assembly, while the vibration frequencies in the lock-in range approach the natural frequency of the assembly. The frequency ratios ($f_h/f_{h,0}$ and $f_\theta/f_{\theta,0}$) shown in the middle and right parts of Fig. 4(c) increase linearly with increasing the reduced velocity outside the lock-in range while they are close to one within the lock-in range. The frequency responses for the $f_{\theta,0}/f_{h,0}$ = 1 assembly are similar to the typical frequency responses for the VIVs of a circular cylinder with a relatively large mass ratio[45].

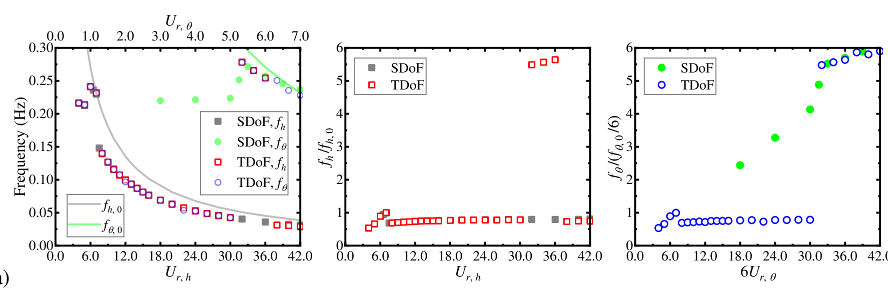

(a)

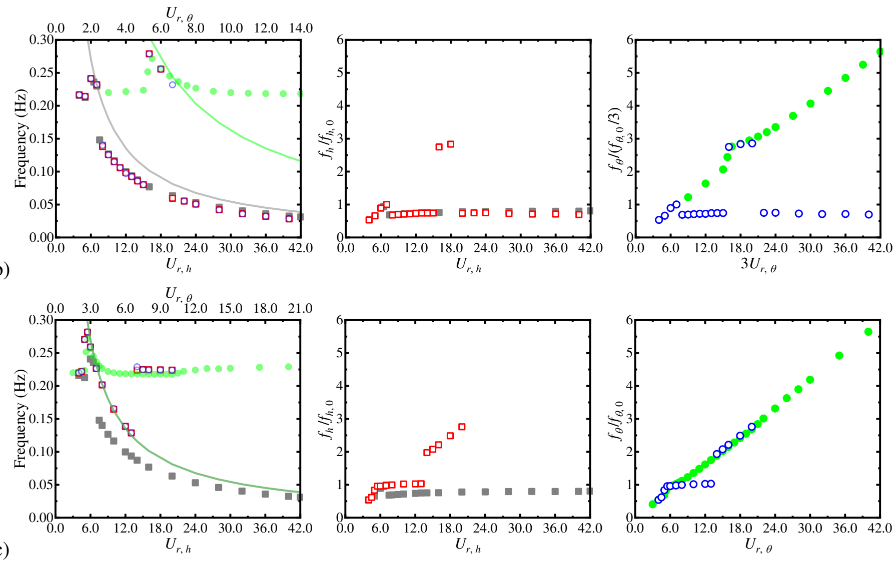

(b)

(c)

FIG. 4. Steady-state vertical and torsional vibration frequencies of cylinder-plate assemblies with various frequency ratios: (a) $f_{\theta,0}/f_{h,0}$ = 6; (b) $f_{\theta,0}/f_{h,0}$ = 3; (c) $f_{\theta,0}/f_{h,0}$ = 1.

Typical displacement time histories of cylinder-plate assemblies with $f_{\theta,0}/f_{h,0}$ = 6, 3, and 1 are shown in Figs. 5, 6, and 7, respectively. In these figures, the blue line represents the dimensionless vertical displacement h/D, the red line represents the torsional displacement θ, the horizontal axis represents time t in second (s), the unit of the vertical axis on the left is 1 for the dimensionless vertical displacement, and the unit of the vertical axis on the right is degree (°) for the torsional displacement. As shown in Fig. 5(a) for the $f_{\theta,0}/f_{h,0}$ = 6 assembly, a well-organised quasi-harmonic vibration with very low vibration amplitudes is developed at a very low reduced velocity of $U_{r,h}$ = 4. At $U_{r,h}$ = 7 shown in Fig. 5(b), the vibration exhibits noticeable fluctuations due to the multiple-frequency components involved in the vibration. The vibration amplitudes remarkably increase at $U_{r,h}$ = 8, and then increase with increasing the reduced velocity until $U_{r,h}$ = 28, as seen from Figs. 5(c) ~ 5(h). The fluctuation in the torsional vibration becomes more serious with increasing the reduced velocity, indicating that significant higher-frequency components exit in the torsional displacement signal. It is noted from Figs. 5(e) ~ 5(h) that for a specific reduced velocity within $U_{r,h}$ = 16 ~ 28, the vibration seems to stay on a steady state at around t = 80 ~ 140 s, after which the vibration amplitudes increase again until a final steady state is achieved. A similar phenomenon has been reported for the VIV of a circular cylinder in the wind tunnel tests of Goswami et al.[46] Zhang et al.[47] suggested that the first steady state might be an unstable limit cycle while the second steady state is a stable limit cycle. Further analyses are required to explain this phenomenon for the TDoF cylinder-plate assembly. At $U_{r,h}$ = 32 shown in Fig. 5(i), the transient stage of the vibration is very long and the steady-state vibration is achieved at around t = 450 s. There is a competition between the vertical and torsional modes, i.e., the vibration is firstly dominated by the vertical vibration at t = 200 ~ 380 s, while the torsional vibration becomes dominant after t = 380 s. The torsional amplitude dramatically increases to a value of θ_{max} = 13.60°, and the vertical amplitude reduces sharply to h_{max} = 0. At $U_{r,h}$ = 34 and 36 shown in Figs. 5(j) an 5(k), the steady-state vibrations are still dominated by the torsional vibrations while the transient stages are shortened. Finally, at $U_{r,h}$ = 40 shown in Fig. 5(l), both vertical and torsional vibrations exist and different frequencies dominate the vibrations in two degrees of freedom. The torsional vibration seems to stay on a steady state at around t = 120 ~ 250 s, while the vertical vibration amplitude continues to increase until $t \approx 400$ s. After $t \approx 400$ s, the vertical vibration behaves as a quasi-harmonic vibration while the torsional vibration exhibits noticeable fluctuations. It is also noted from Figs. 5(i) ~ 5(l) that, within the lock-in range for torsional VIVs, the torsional displacements grow rapidly in a short period while the vertical displacements fluctuate in a much larger time scale. A possible explanation is that the dominant torsional frequencies are much higher than the vertical torsional frequencies.

As seen from Figs. 5 and 6, the displacement responses for the $f_{\theta,0}/f_{h,0}$ = 6 and $f_{\theta,0}/f_{h,0}$ = 3 assemblies are similar for a specific torsional reduced flow velocity $U_{r,\theta}$. For example, there is a competition between the vertical and torsional modes for the $f_{\theta,0}/f_{h,0}$ = 6 assembly at $U_{r,h} = 6U_{r,\theta}$ = 32 and for the $f_{\theta,0}/f_{h,0}$ = 3 assembly at $U_{r,h} = 3U_{r,\theta}$ = 16, as seen from Figs. 5(i) and 6(f). For the $f_{\theta,0}/f_{h,0}$ = 6 assembly at $U_{r,h} = 6U_{r,\theta}$ = 40 and for the $f_{\theta,0}/f_{h,0}$ = 3 assembly at $U_{r,h} = 3U_{r,\theta}$ = 20, the vertical and torsional vibrations are dominated by different frequencies, as shown in Figs. 5(l) and 6(h). However, with further increasing the reduced velocity (e.g., $U_{r,h} = 3U_{r,\theta}$ = 24 ~ 36 for the $f_{\theta,0}/f_{h,0}$ = 3 assembly, as shown in Fig. 6(i) ~ 6(l)), different frequencies dominate the vertical and torsional vibrations at the transient stage while they are dominated by the same frequency (that is close to the vertical natural frequency) at the steady-state stage.

Fig. 7 presents typical displacement histories of the $f_{\theta,0}/f_{h,0}$ = 1 assembly. Quasi-harmonic vibrations are observed in the lock-in range, e.g., $U_{r,h} = U_{r,\theta}$ = 6, 12, and 14, as shown in Figs. 7(b) ~ (d). The assembly vibrates around a non-zero equilibrium angle at higher reduced velocities, e.g., $U_{r,h} = U_{r,\theta}$ = 20 and 24, as given in Figs. 7(e) and (f). According to Zhang et al.[41], the symmetry-breaking bifurcation is induced by the combined influences of the spring restoring moment and the flow-induced moment. In the considered range of reduced velocities, the symmetry-breaking bifurcation occurs only for the $f_{\theta,0}/f_{h,0}$ = 1 assembly since its torsional stiffness is much lower than other assemblies so that the flow-induced moment is able to surpass the spring restoring moment.

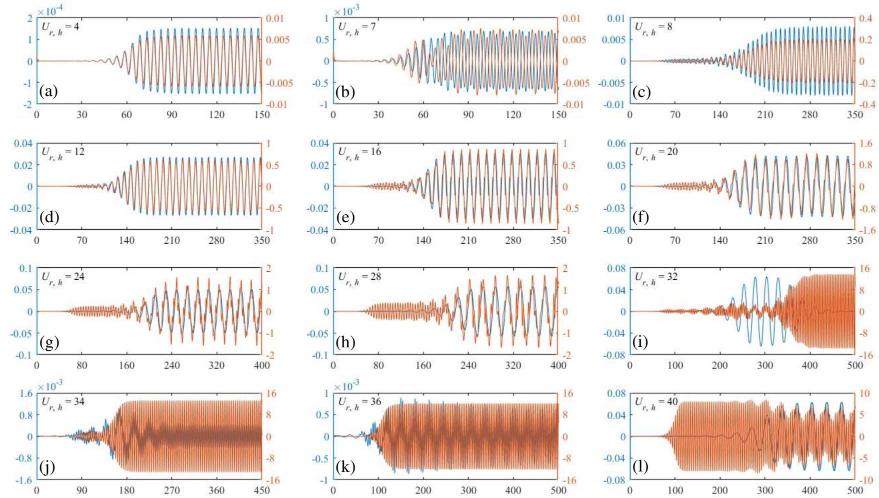

FIG. 5. Displacement signals of cylinder-plate assembly with $f_{\theta,0}/f_{h,0}$ = 6: (a) $U_{r,h}$ = 4; (b) $U_{r,h}$ = 7; (c) $U_{r,h}$ = 8; (d) $U_{r,h}$ = 12; (e) $U_{r,h}$ = 16; (f) $U_{r,h}$ = 20; (g) $U_{r,h}$ = 24; (h) $U_{r,h}$ = 28; (i) $U_{r,h}$ = 32; (j) $U_{r,h}$ = 34; (k) $U_{r,h}$ = 36; (l) $U_{r,h}$ = 40. The blue lines show dimensionless vertical displacements, while the red lines show torsional displacements. The horizontal axes are time in seconds. The left vertical axes are dimensionless vertical displacements, while the right vertical axes are torsional displacements in degrees (°).

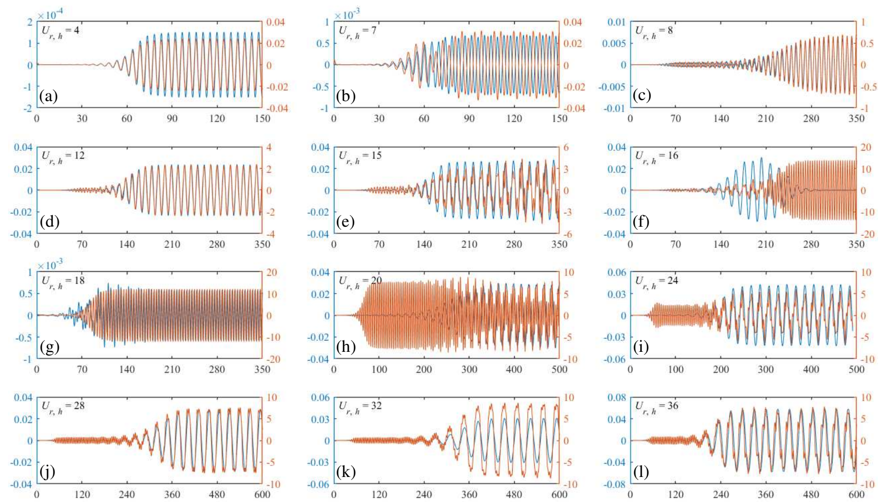

FIG. 6. Displacement signals of cylinder-plate assembly with $f_{\theta,0}/f_{h,0}$ = 3: (a) $U_{r,h}$ = 4; (b) $U_{r,h}$ = 7; (c) $U_{r,h}$ = 8; (d) $U_{r,h}$ = 12; (e) $U_{r,h}$ = 15; (f) $U_{r,h}$ = 16; (g) $U_{r,h}$ = 18; (h) $U_{r,h}$ = 20; (i) $U_{r,h}$ = 24; (j) $U_{r,h}$ = 28; (k) $U_{r,h}$ = 32; (l) $U_{r,h}$ = 36. The blue lines show dimensionless vertical displacements, while the red lines show torsional displacements. The horizontal axes are time in seconds. The left vertical axes are dimensionless vertical displacements, while the right vertical axes are torsional displacements in degrees (°).

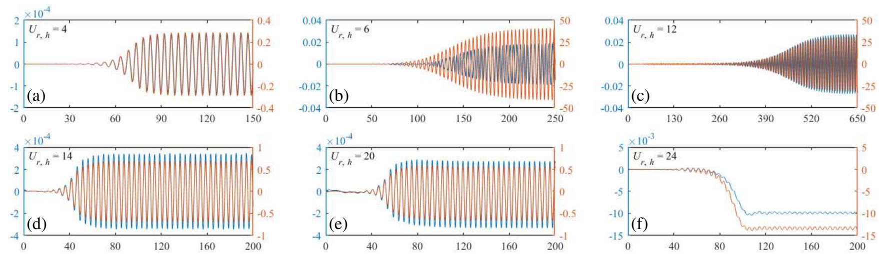

FIG. 7. Displacement signals of cylinder-plate assembly with $f_{\theta,0}/f_{h,0}$ = 1: (a) $U_{r,h}$ = 4; (b) $U_{r,h}$ = 6; (c) $U_{r,h}$ = 12; (d) $U_{r,h}$ = 14; (e) $U_{r,h}$ = 20; (f) $U_{r,h}$ = 24. The blue lines show dimensionless vertical displacements, while the red lines show torsional displacements. The horizontal axes are time in seconds. The left vertical axes are dimensionless vertical displacements, while the right vertical axes are torsional displacements in degrees (°).

B. Flow-induced forces

Fig. 8 presents the mean values of the flow-induced drag force coefficients ($C_{D,\text{mean}}$), and the standard deviations of the lift force ($C_{L,\text{std}}$) and torsional moment coefficients ($C_{M,\text{std}}$) for the cylinder-plate assemblies with various frequency ratios. The results for the SDoF vertical assembly and the SDoF torsional assembly are plotted for comparison. In addition, the mean drag coefficients for a stationary circular cylinder and a stationary cylinder-plate assembly are also given.

It can be seen from Figs. 8(a) and 8(b) that for cylinder-plate assemblies with $f_{\theta,0}/f_{h,0}$ = 6 and 3, the force coefficients are close to those of the SDoF vertical assembly in the V branch while the difference increases with decreasing the frequency ratio. This is expected since torsional vibration also exists in the V branch, and the torsional amplitude increases with decreasing the frequency ratio, as seen from Fig. 3. On the other hand, the vibration in the T branch is dominated by the torsional vibration, while the vertical vibration amplitude is almost zero (see Fig. 3). Hence, the force coefficients for TDoF cylinder-plate assemblies in the T branch are almost identical to those of the SDoF torsional assembly. In the C branch, the force coefficients for the $f_{\theta,0}/f_{h,0}$ = 6 cylinder-plate assembly are close to those of the SDoF vertical assembly, as shown in Fig. 8(a). However, the force coefficients for TDoF cylinder-plate assemblies in the C branch move towards the values for the SDoF torsional assembly with decreasing the frequency ratio, as seen from Figs. 8(b). This is also expected since the ratio between the torsional and vertical amplitudes in the T brach increases with decreasing the frequency ratio, as noticed from Fig. 3(a) ~ 3(d).

For the TDoF assembly with $f_{\theta,0}/f_{h,0}$ = 6, the mean drag coefficient increases with increasing the reduced velocity within $U_{r,h}$ = 6 ~ 14, and then decreases with increasing the reduced velocity. The mean drag coefficient exhibits two peak values in the vertical and torsional lock-in ranges, respectively. The results are supported by some previous observations that VIV is accompanied by a more significant increase of the mean drag coefficient compared with galloping. For the TDoF assembly with $f_{\theta,0}/f_{h,0}$ = 3, the mean drag coefficient at a lower reduced velocity (e.g., $U_{r,h}$ = 6 ~ 14) is lower than the SDoF vertical assembly due to the reduced vertical vibration, while the mean drag coefficient at a higher reduced velocity (e.g., $U_{r,h}$ = 18 ~ 42) is higher than the SDoF torsional assembly due to the accompanied vertical motion. For both TDoF assemblies, the maximum mean drag coefficients are accompanied by the maximum torsional vibration amplitudes. The maximum value of the mean drag coefficient seems almost independent of the frequency ratio since the maximum torsional vibration amplitude remains almost unchanged with varying the frequency ratio. For all reduced flow velocities, the mean drag coefficients of the $f_{\theta,0}/f_{h,0}$ = 6 and 3 cylinder-plate assemblies are lower than that of a stationary circular cylinder. The standard deviations of the lift and moment coefficients ($C_{L,\text{ std}}$ and $C_{M,\text{ std}}$) are very small at lower reduced velocities. $C_{L,\text{ std}}$ and $C_{M,\text{ std}}$ then exhibit a sharp increase and a sharp drop. After these sharp jumps, $C_{L,\text{ std}}$ and $C_{M,\text{ std}}$ decrease with increasing the reduced velocity with a discontinuity in the torsional lock-in range. The peak values of $C_{L,\text{ std}}$ and $C_{M,\text{ std}}$ decrease with increasing the frequency ratio.

For the $f_{\theta,0}/f_{h,0}$ = 1 cylinder-plate assembly given in Fig. 8(c), the force coefficients almost remain unchanged outside the lock-in range while the coefficients are larger within the lock-in range. In this lock-in range, the mean drag coefficients for the $f_{\theta,0}/f_{h,0}$ = 1 assembly are considerably larger than those of the SDoF assemblies and the stationary circular cylinder. However, despite the very large torsional vibration amplitude, $C_{L,\text{ std}}$ and $C_{M,\text{ std}}$ are generally lower than those of the SDoF vertical assembly with some exceptions at the beginning of the lock-in range.

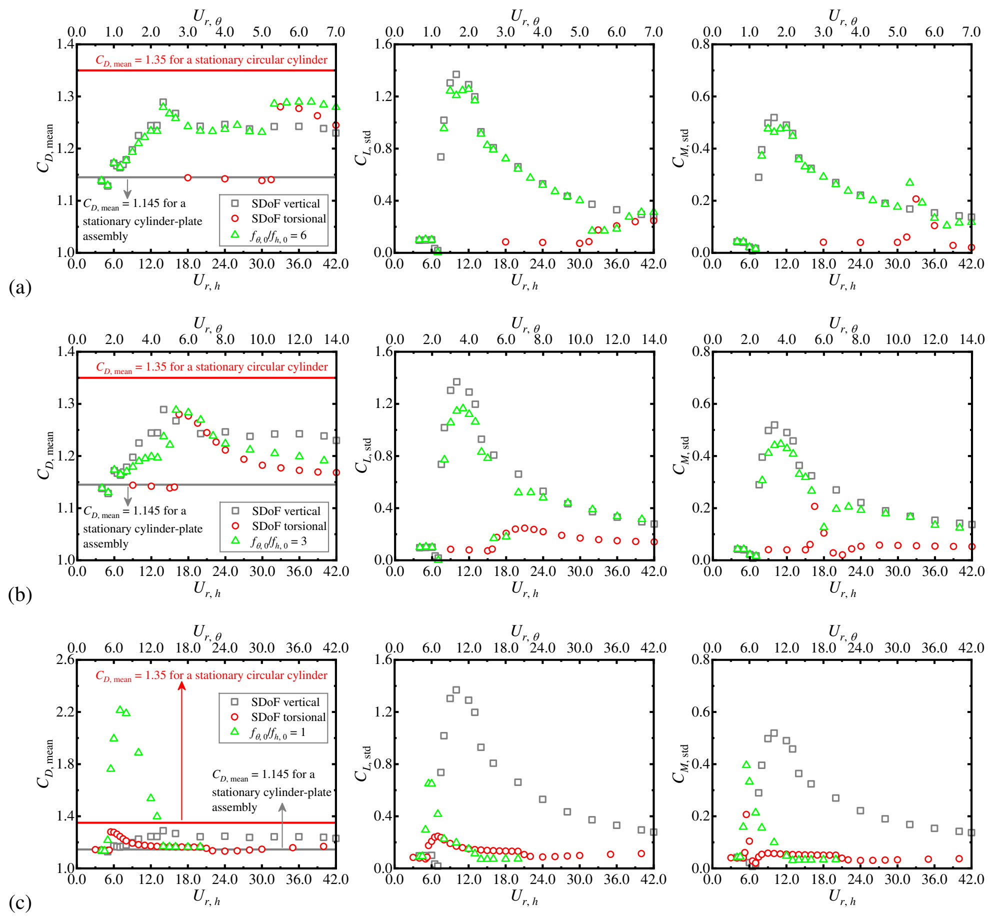

FIG. 8. Flow-induced force coefficients of cylinder-plate assemblies with various frequency ratios: (a) $f_{\theta,0}/f_{h,0}$ = 6; (b) $f_{\theta,0}/f_{h,0}$ = 3; (c) $f_{\theta,0}/f_{h,0}$ = 1.

Fig. 9 shows the steady-state displacement signals (h/D and θ) and flow-induced force coefficients (C_D, C_L, and C_M) for five typical cases. In these figures, the solid blue line represents the displacement or force coefficients of the cylinder-plate assembly, while the dashed green and dashed red lines represent the force coefficients of the circular cylinder and the splitter plater, respectively. The drag coefficient of the splitter plate is close to zero, and the result for each case is the actual value added by 1.2. The three cases of the $f_{\theta,0}/f_{h,0}$ = 6 cylinder-plate assembly in Figs. 9(a) ~ (c), i.e., U_r = 12, 34, and 40, are representatives in the V branch, T branch, and C branch, respectively. The case of $f_{\theta,0}/f_{h,0}$ = 3 and U_r = 24 in Fig. 9(d) is another representative in the C branch. The former representative ($f_{\theta,0}/f_{h,0}$ = 6 and U_r = 40) in the C branch is characterised by different dominant frequencies of the vertical and torsional vibrations, while the latter one ($f_{\theta,0}/f_{h,0}$ = 3 and U_r = 24) is characterised by the same dominant frequency of the vertical and torsional vibrations. The case of $f_{\theta,0}/f_{h,0}$ = 1 and U_r = 24 is a representative after the symmetry-breaking bifurcation. These cases are referred to as Case 1 ~ 5 in the following parts.

As seen from Figs. 9(a), 9(b), 9(d), and 9(e), the dominant frequency of the lift force and torsional moment of Case 1, 2, 4, or 5 are the same as the vibration frequency. Since the assembly vibrates symmetrically around its original equilibrium position, the vortices shedding from alternate sides of the assembly have the same effects on the drag force; hence, the dominant frequency of the drag force is twice the vibration frequency. For an asymmetric case (that vibrates around a non-zero equilibrium angle), the effects of vortices shedding from alternate sides on the drag force are different, and hence the dominant frequency of the drag force is consistent with the vibration frequency. For Case 3 (which is also a symmetric case), the dominant frequency of the lift force and the torsional moment is equal to the vertical vibration frequency, and the dominant frequency of the drag force is twice the vertical vibration frequency. However, remarkable higher-frequency components are observed due to the high torsional vibration frequency. The mechanism for these higher-frequency components will be explained later in subsection IV.D. Another observation from Fig. 9 is that the torsional moment on the assembly is mainly contributed by the moment on the splitter plate. The torsional moment is mainly produced by the pressure difference between two surfaces of the splitter plate, while the pressure on the surface of the circular cylinder cannot produce any torsional moment. Some pressure contours on the surfaces of the plate for an SDoF torsional assembly can be found in Zhang et al.[41]

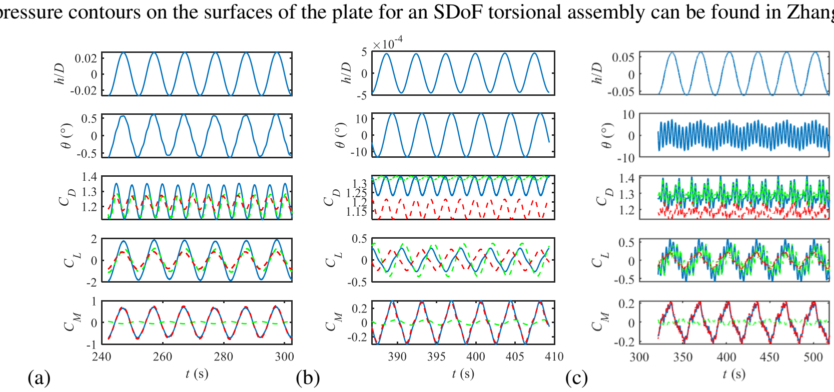

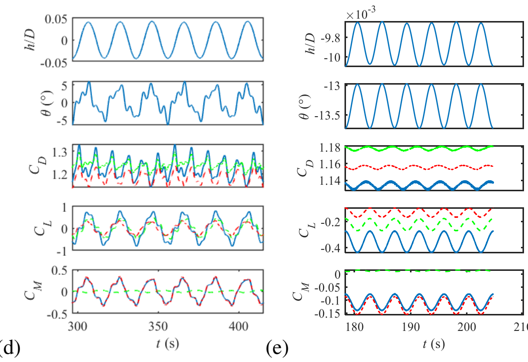

(d) (e)

FIG. 9. Time histories of displacements and force coefficients of cylinder-plate assembly: (a) Case 1, $f_{\theta,0}/f_{h,0}$ = 6 and $U_{r,h}$ = 12; (b) Case 2, $f_{\theta,0}/f_{h,0}$ = 6 and $U_{r,h}$ = 34; (c) Case 3, $f_{\theta,0}/f_{h,0}$ = 6 and $U_{r,h}$ = 40; (d) Case 4, $f_{\theta,0}/f_{h,0}$ = 3 and $U_{r,h}$ = 24; (e) Case 5, $f_{\theta,0}/f_{h,0}$ = 1 and $U_{r,h}$ = 24. Solid blue line: displacement or force coefficient of cylinder-plate assembly; dashed green line: force coefficient of circular cylinder; dashed red line: force coefficient of splitter plater.

C. Phase difference between displacements and forces

Fig. 10 shows the phase difference ϕ_h between the lift force and vertical displacement, and the phase difference ϕ_θ between the torsional moment and torsional displacement for circular-cylinder assemblies with $f_{\theta,0}/f_{h,0}$ = 6, $f_{\theta,0}/f_{h,0}$ = 3, and $f_{\theta,0}/f_{h,0}$ = 1. The results for the SDoF vertical assembly and the SDoF torsional assembly are also given for comparison.

As shown in Fig. 10 (a) and 10(b), ϕ_h is approximately 0° at lower reduced flow velocities for assemblies with $f_{\theta,0}/f_{h,0}$ = 6 and 3. ϕ_h jumps to 180° at $U_{r,h}$ = 7 and then drops back to 0°. The phase jump is also observed for the SDoF vertical assembly by Sun et al.[31] ϕ_h remains around 0° with increasing reduced flow velocity until a 180° phase jump occurs in the T branch. ϕ_h jumps back to and remains around 0° in the C branch. For assemblies with $f_{\theta,0}/f_{h,0}$ = 6 and 3, ϕ_θ is around 0° throughout the considered range of reduced flow velocities. The phase jump is induced by the changing of the timing and strength of the flow field (which is largely affected by the assembly vibration), as discussed in detail in other papers[41, 48]. Since the frequency ratio affects the assembly vibration significantly, the phase jump is also remarkably influenced by the frequency ratio.

For the $f_{\theta,0}/f_{h,0}$ = 1 circular-cylinder assembly, ϕ_h and ϕ_θ are around 0° at lower reduced flow velocities. ϕ_h and ϕ_θ jump to 180° at around $U_{r,h}$ = 10 and then remains around 180° for higher reduced velocities. The phase responses are similar to the typical phase responses of VIVs of a circular cylinder.[49]

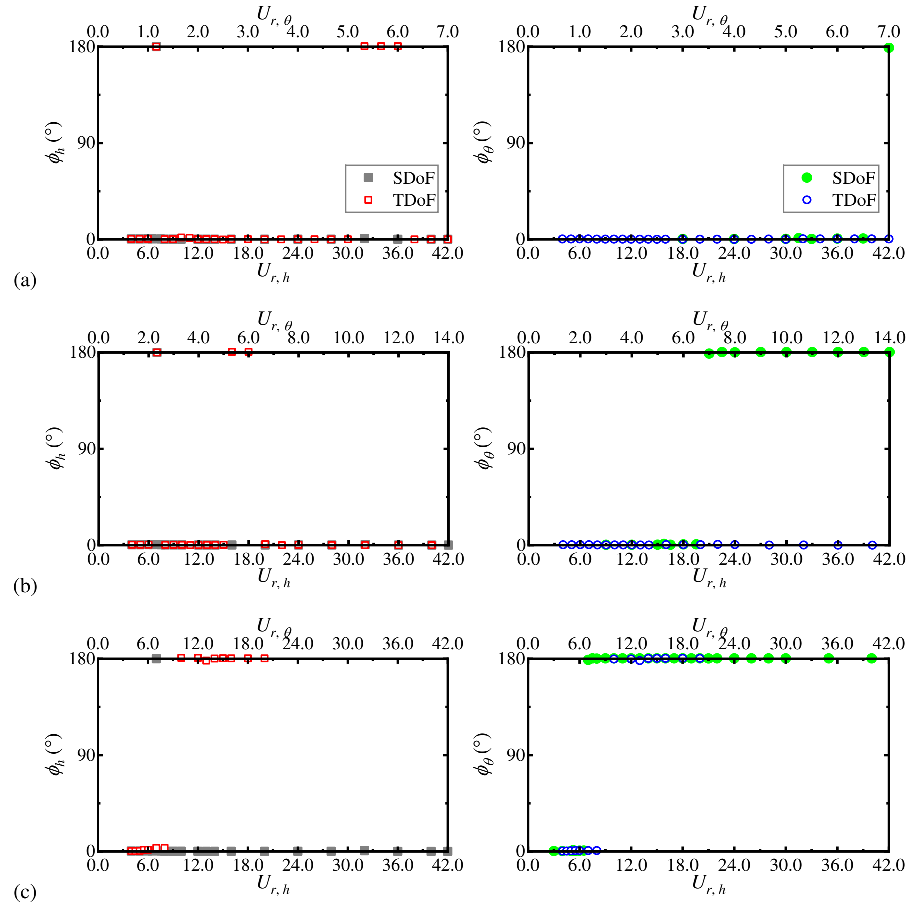

FIG. 10. Phase differences between lift force and vertical displacement, and between torsional moment and torsional displacement for circular-cylinder assemblies with various frequency ratios: (a) $f_{\theta,0}/f_{h,0}$ = 6; (b) $f_{\theta,0}/f_{h,0}$ = 3; (c) $f_{\theta,0}/f_{h,0}$ = 1.

D. Flow pattern

Fig. 11 shows the instantaneous vorticity fields for Case 1 ~ 5. The instantaneous vorticity fields are given at eight time instants within one vibration cycle T for each case. The first image (i.e., t = 0) for each case corresponds to a time instant when the cylinder-plate assembly moves down past the equilibrium position. The assembly then moves to the lowest position at t = 2T/8 and back to the equilibrium position at t = 4T/8. Then, the assembly moves to the highest position at t = 6T/8 and back to the equilibrium position at t = T.

As shown in the figures, the formation length of the vortices for Case 1 in the V branch is relatively longer than those of other cases. For Case 1, as presented in Fig. 11(a), the lower vortex reattaches to the tip of the splitter plate as the assembly moves downward. A downward lift force is thus created, which drives the assembly into a large amplitude vibration. A similar process repeats during the upward motion of the assembly so that a continuous vibration is excited. The mechanism mentioned above for large vertical vibration of the circular-plate assembly is similar to that of a circular cylinder with a fixed fairing.[50, 51] The 2P vortex mode[52] is formed in the wake, i.e., two pairs of vortices shed alternately within one vibration cycle. The vortex mode is consistent with that during the vibration of the SDoF vertical assembly.[31] Since the formation length is very large, the vortex sheddings do not significantly influence the flow-induced forces of the assembly.

The vortex formation length is largely shortened in the T branch, as shown in Fig. 11(b) for Case 2. The 2S vortex mode[52] is formed, i.e., two single vortices shed alternately within one vibration cycle. The vortex mode is consistent with that during the vibration of the SDoF torsional assembly.[40, 41] This is expected since the torsional vibration is dominant in the T branch. The torsional vibration of the assembly is mainly driven by the alternative vortex shedding in its wake.

As seen from Fig. 11(c), the formation length for Case 3 in the C branch is longer than that for Case 2 in the T branch. Therefore, the flow-induced forces are mainly influenced by the interaction between the assembly and the shear layers. Hence, the dominant frequency of the lift force and torsional moment equals the vibration frequency. Since the torsional vibration frequency is eight times the vertical vibration frequency (see Fig. 4(a)), eight pairs of vortices are formed and shed during one vibration cycle. These vortices contribute to remarkable higher-frequency components in the flow-induced forces, as shown in Fig. 9(c).

As shown in Fig. 11(d), the formation length for Case 4 in the C branch is longer than that for Case 2. The flow-induced forces are mainly contributed by the interaction between the assembly and the shear layers. Five pairs of vortices are formed and shed during one vibration cycle. Spectral analysis of the torsional displacement shows that there is a peak at f and a secondary peak at $5f$, where $f = f_h = f_\theta$ is the dominant vibration frequency. These vortices result in significant higher-frequency components in the flow-induced forces, as shown in Fig. 9(d).

The 2S vortex mode is observed for the $f_{\theta,0}/f_{h,0}$ = 1 assembly for all considered reduced flow velocities. Fig. 11(e) shows the vortex mode at $U_{r,h}$ = 24 after the symmetry-breaking bifurcation. The vortex mode for the $f_{\theta,0}/f_{h,0}$ = 1 assembly is similar to that for the SDoF torsional assembly.[40, 41]

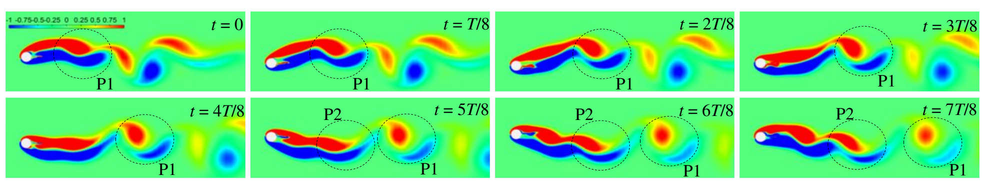

(a)

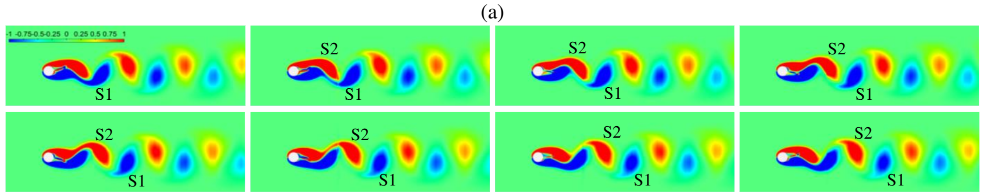

(b)

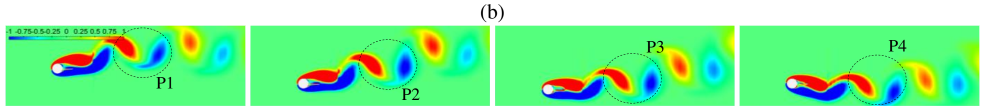

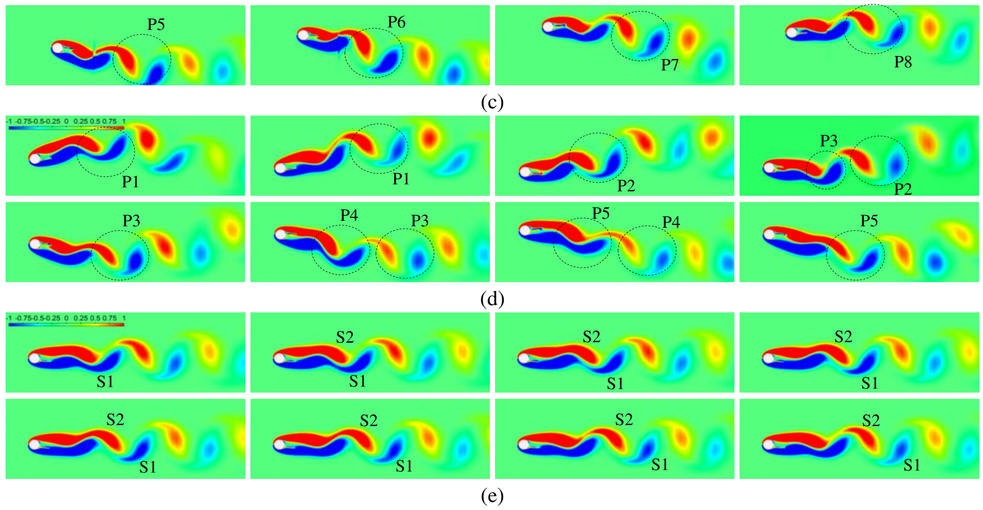

FIG. 11. Instantaneous vorticity fileds within one vibration cycle: (a) Case 1, $f_{\theta,0}/f_{h,0}$ = 6 and $U_{r,h}$ = 12; (b) Case 2, $f_{\theta,0}/f_{h,0}$ = 6 and $U_{r,h}$ = 34; (c) Case 3, $f_{\theta,0}/f_{h,0}$ = 6 and $U_{r,h}$ = 40; (d) Case 4, $f_{\theta,0}/f_{h,0}$ = 3 and $U_{r,h}$ = 24; (e) Case 5, $f_{\theta,0}/f_{h,0}$ = 1 and $U_{r,h}$ = 24.

V. Conclusions

Numerical simulations were presented to investigate the flow-induced vibrations of a circular cylinder with an attached splitter plate at a Reynolds number of 100. The cylinder-plate assembly was elastically mounted in the vertical, in-line, and torsional degrees of freedom. Simulations were conducted at reduced flow velocities of $U_{r,h}$ = 2 ~ 42 for five torsional-to-vertical frequency ratios, i.e., $f_{\theta,0}/f_{h,0}$ = 6, 4, 3, 2, and 1. For assemblies with $f_{\theta,0}/f_{h,0}$ = 6 ~ 2, the vibrations can be divided into three branches, i.e., a vertical vibration-dominated branch (V branch), a torsional vibration-dominated branch (T branch), and a coupled vibration-dominated branch (C branch). In the V branch, vertical vibration is dominant, while remarkable torsional vibration also exists. The vertical vibration amplitude of the TDoF (three-degree-of-freedom) assembly is lower than that of the SDoF (single-degree-of-freedom) vertical assembly at the same reduced velocity, and the difference increases with decreasing the frequency ratio. The nearly SDoF torsional vibration in the T branch is almost identical to the vibration of the SDoF torsional assembly at the same reduced flow velocity. The vibration in the C branch is a vertical-torsional coupled vibration, and the ratio between the torsional and vertical amplitudes increases with decreasing the frequency ratio. For assemblies with $f_{\theta,0}/f_{h,0}$ = 1, vertical-torsional coupled VIVs were observed with the largest torsional amplitude as high as 46.3°.

For cylinder-plate assemblies with $f_{\theta,0}/f_{h,0}$ = 6 ~ 2 in the T branch, the flow-induced force coefficients are almost identical to those of the SDoF torsional assembly at the same reduced flow velocity. In the V and C branches, the force coefficients are close to those of the SDoF vertical assembly, while the difference increases with decreasing the frequency ratio. The mean drag coefficients for the $f_{\theta,0}/f_{h,0}$ = 6 ~ 2 assemblies are lower than that of a stationary circular cylinder but often higher than that of a stationary cylinder-plate assembly. The mean drag coefficients for the $f_{\theta,0}/f_{h,0}$ = 1 assembly in the lock-in range are considerably larger than that of the stationary circular cylinder.

The unsteady lift force and torsional moment coefficients for the $f_{\theta,0}/f_{h,0}$ = 1 assembly are generally lower than those of the SDoF vertical assembly despite the very large torsional vibration amplitudes.

For cylinder-plate assemblies with $f_{\theta,0}/f_{h,0}$ = 6 ~ 2, the V branch and C branch vibrations are accompanied by larger formation lengths of the vortices, while the T branch vibrations are accompanied by shorter formation lengths. Hence, the effects of the interaction between the assembly and the shear layers are more significant in the V and C branches than in the T branch. The VIVs for the $f_{\theta,0}/f_{h,0}$ = 1 assembly are accompanied by the typical 2S mode of vortex shedding.

Acknowledgments

The authors gratefully acknowledge the support of their partners Equinor Energy AS, ConocoPhillips Skandinavia AS, NTNU, SINTEF, and the Research Council of Norway (strategic Norwegian research program PETROMAKS2, grant agreement number 280713).

Data availability

The data that support the findings of this study are available from the corresponding author upon reasonable request.

References

1. H. Zhu, Y. Gao, and H. Zhao, "Experimental investigation on the flow-induced vibration of a free-hanging flexible riser by internal unstable hydrodynamic slug flow," Ocean Engineering **164**, 488 (2018).

2. J.-n. Song, L. Lu, B. Teng, H.-i. Park, G.-q. Tang, and H. Wu, "Laboratory tests of vortex-induced vibrations of a long flexible riser pipe subjected to uniform flow," Ocean engineering **38**, 1308 (2011).

3. M. Jafari, F. Hou, and A. Abdelkefi, "Wind-induced vibration of structural cables," Nonlinear Dynamics **100**, 351 (2020).

4. W. Chen, D. Gao, H. Li, and H. Hu, "Wake-flow-induced vibrations of vertical hangers behind the tower of a long-span suspension bridge," Engineering Structures **169**, 188 (2018).

5. F. Xu, H. Yu, M. Zhang, and Y. Han, "Experimental study on aerodynamic characteristics of a large-diameter ice-accreted cylinder without icicles," Journal of Wind Engineering and Industrial Aerodynamics **208**, 104453 (2021).

6. F. Xu, and H. Yu, "Effect of Ice Accretion on the Aerodynamic Responses of a Pipeline Suspension Bridge," Journal of Bridge Engineering **25**, 04020091 (2020).

7. M. Zhang, and O. Øiseth, "Convolution-based time-domain simulation for fluidelastic instability in tube arrays," Nonlinear Dynamics 1 (2021).

8. H. Deng, G. Skaugen, E. Næss, M. Zhang, and O. A. Øiseth, "A novel methodology for design optimization of heat recovery steam generators with flow-induced vibration analysis," Energy **226**, 120325 (2021).

9. H. Yu, and M. Zhang, "Effects of side ratio on energy harvesting from transverse galloping of a rectangular cylinder," Energy **226**, 120420 (2021).

10. J. Wang, L. Geng, L. Ding, H. Zhu, and D. Yurchenko, "The state-of-the-art review on energy harvesting from flow-induced vibrations," Applied Energy **267**, 114902 (2020).

11. M. Zhang, A. Abdelkefi, H. Yu, X. Ying, O. Gaidai, and J. Wang, "Predefined angle of attack and corner shape effects on the effectiveness of square-shaped galloping energy harvesters," Applied Energy **302**, 117522 (2021).

12. H. Zhu, T. Tang, H. Zhao, and Y. Gao, "Control of vortex-induced vibration of a circular cylinder using a pair of air jets at low Reynolds number," Physics of Fluids **31**, 043603 (2019).

13. G. Hu, K. T. Tse, M. Wei, R. Naseer, A. Abdelkefi, and K. Kwok, "Experimental investigation on the efficiency of circular cylinder-based wind energy harvester with different rod-shaped attachments," Applied energy **226**, 682 (2018).

14. C. Demartino, and F. Ricciardelli, "Aerodynamics of nominally circular cylinders: A review of experimental results for Civil Engineering applications," Engineering Structures **137**, 76 (2017).

15. G. Hu, K. T. Tse, K. C. S. Kwok, J. Song, and Y. Lyu, "Aerodynamic modification to a circular cylinder to enhance the piezoelectric wind energy harvesting," Applied Physics Letters **109**, 193902 (2016).

16. L. Lu, J.-M. Qin, B. Teng, and Y.-C. Li, "Numerical investigations of lift suppression by feedback rotary oscillation of circular cylinder at low Reynolds number," Physics of Fluids **23**, 033601 (2011).

17. D. Gao, Y. Huang, W.-L. Chen, G. Chen, and H. Li, "Control of circular cylinder flow via bilateral splitter plates," Physics of Fluids **31**, 057105 (2019).

18. H. Zhu, and K. Wang, "Wake adjustment and vortex-induced vibration of a circular cylinder with a C-shaped plate at a low Reynolds number of 100," Physics of Fluids **31**, 103602 (2019).

19. Y. Jin, J.-T. Kim, L. Hong, and L. P. Chamorro, "Flow-induced oscillations of low-aspect-ratio flexible plates with various tip geometries," Physics of Fluids **30**, 097102 (2018).

20. A. Roshko, "On the drag and shedding frequency of two-dimensional bluff bodies," (1954).

21. P. Bearman, "Investigation of the flow behind a two-dimensional model with a blunt trailing edge and fitted with splitter plates," Journal of fluid mechanics **21**, 241 (1965).

22. J. Gerrard, "The mechanics of the formation region of vortices behind bluff bodies," Journal of fluid mechanics **25**, 401 (1966).

23. E. Anderson, and A. Szewczyk, "Effects of a splitter plate on the near wake of a circular cylinder in 2 and 3-dimensional flow configurations," Experiments in Fluids **23**, 161 (1997).

24. C. Apelt, G. West, and A. A. Szewczyk, "The effects of wake splitter plates on the flow past a circular cylinder in the range 104< R< 5× 104," Journal of Fluid Mechanics **61**, 187 (1973).

25. B. G. Dehkordi, and H. H. Jafari, "On the suppression of vortex shedding from circular cylinders using detached short splitter-plates," Journal of fluids engineering **132**, (2010).

26. J.-Y. Hwang, K.-S. Yang, and S.-H. Sun, "Reduction of flow-induced forces on a circular cylinder using a detached splitter plate," Physics of Fluids **15**, 2433 (2003).

27. S. Ozono, "Flow control of vortex shedding by a short splitter plate asymmetrically arranged downstream of a cylinder," Physics of Fluids **11**, 2928 (1999).

28. H. Kawai, "A discrete vortex analysis of flow around a vibrating cylinder with a splitter plate," Journal of Wind Engineering and Industrial Aerodynamics **35**, 259 (1990).

29. Y. Nakamura, K. Hirata, and K. Kashima, "Galloping of a circular cylinder in the presence of a splitter plate," Journal of fluids and structures **8**, 355 (1994).

30. B. Stappenbelt, "Splitter-plate wake stabilisation and low aspect ratio cylinder flow-induced vibration mitigation," International Journal of Offshore and Polar Engineering **20**, (2010).

31. X. Sun, C. S. Suh, Z.-H. Ye, and B. Yu, "Dynamics of a circular cylinder with an attached splitter plate in laminar flow: A transition from vortex-induced vibration to galloping," Physics of Fluids **32**, 027104 (2020).

32. S. Liang, J. Wang, and Z. Hu, "VIV and galloping response of a circular cylinder with rigid detached splitter plates," Ocean Engineering **162**, 176 (2018).

33. G. R. Assi, and P. W. Bearman, "Transverse galloping of circular cylinders fitted with solid and slotted splitter plates," Journal of Fluids and Structures **54**, 263 (2015).

34. T. R. Sahu, M. Furquan, Y. Jaiswal, and S. Mittal, "Flow-induced vibration of a circular cylinder with rigid splitter plate," Journal of Fluids and Structures **89**, 244 (2019).

35. H. Zhu, G. Li, and J. Wang, "Flow-induced vibration of a circular cylinder with splitter plates placed upstream and downstream individually and simultaneously," Applied Ocean Research **97**, 102084 (2020).

36. F. Huera-Huarte, "On splitter plate coverage for suppression of vortex-induced vibrations of flexible cylinders," Applied Ocean Research **48**, 244 (2014).

37. J. M. Cimbala, and K. Chen, "Supercritical Reynolds number experiments on a freely rotatable cylinder/splitter plate body," Physics of Fluids **6**, 2440 (1994).

38. J. M. Cimbala, and S. Garg, "Flow in the wake of a freely rotatable cylinder with splitter plate," AIAA journal **29**, 1001 (1991).

39. J. Xu, M. Sen, and M. Gad-el-Hak, "Dynamics of a rotatable cylinder with splitter plate in uniform flow," Journal of fluids and structures **7**, 401 (1993).

40. L. Lu, X.-l. Guo, G.-q. Tang, M.-m. Liu, C.-q. Chen, and Z.-h. Xie, "Numerical investigation of flow-induced rotary oscillation of circular cylinder with rigid splitter plate," Physics of Fluids **28**, 093604 (2016).

41. M. Zhang, X. Wang, and O. Øiseth, "Torsional vibration of a circular cylinder with an attached splitter plate in laminar flow," Ocean Engineering **236**, 109514 (2021).

42. X. Ying, F. Xu, M. Zhang, and Z. Zhang, "Numerical explorations of the limit cycle flutter characteristics of a bridge deck," Journal of Wind Engineering and Industrial Aerodynamics **169**, 30 (2017).

43. M. Zhang, F. Xu, Z. Zhang, and X. Ying, "Energy budget analysis and engineering modeling of post-flutter limit cycle oscillation of a bridge deck," Journal of Wind Engineering and Industrial Aerodynamics **188**, 410 (2019).

44. M. Zhang, F. Xu, and Y. Han, "Assessment of wind-induced nonlinear post-critical performance of bridge decks," Journal of Wind Engineering and Industrial Aerodynamics **203**, 104251 (2020).

45. C. Williamson, and R. Govardhan, "Vortex-induced vibrations," Annu. Rev. Fluid Mech. **36**, 413 (2004).

46. I. Goswami, R. H. Scanlan, and N. P. Jones, "Vortex-induced vibration of circular cylinders. I: experimental data," Journal of Engineering Mechanics **119**, 2270 (1993).

47. M. Zhang, T. Wu, and F. Xu, "Vortex-induced vibration of bridge decks: describing function-based model," Journal of Wind Engineering and Industrial Aerodynamics **195**, 104016 (2019).

48. T. Prasanth, and S. Mittal, "Vortex-induced vibrations of a circular cylinder at low Reynolds numbers," Journal of Fluid Mechanics **594**, 463 (2008).

49. A. Khalak, and C. H. Williamson, "Motions, forces and mode transitions in vortex-induced vibrations at low mass-damping," Journal of fluids and Structures **13**, 813 (1999).

50. H. Zheng, and J. Wang, "Numerical study of galloping oscillation of a two-dimensional circular cylinder attached with fixed fairing device," Ocean Engineering **130**, 274 (2017).

51. G. R. Assi, P. Bearman, and N. Kitney, "Low drag solutions for suppressing vortex-induced vibration of circular cylinders," Journal of Fluids and Structures **25**, 666 (2009).

52. C. H. Williamson, and A. Roshko, "Vortex formation in the wake of an oscillating cylinder," Journal of fluids and structures **2**, 355 (1988).

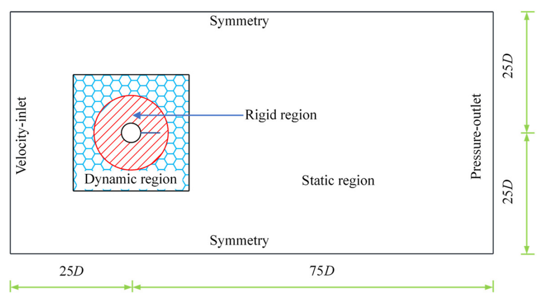

FIG. 1. Model configuration, computational domain, and boundary conditions.

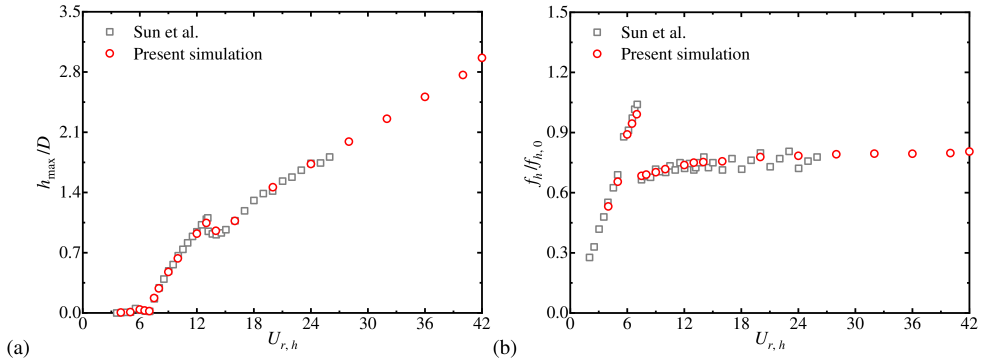

FIG. 2. Comparison between present results and the results of Sun et al.[31]: (a) vertical vibration amplitude and (b) vertical vibration frequency.

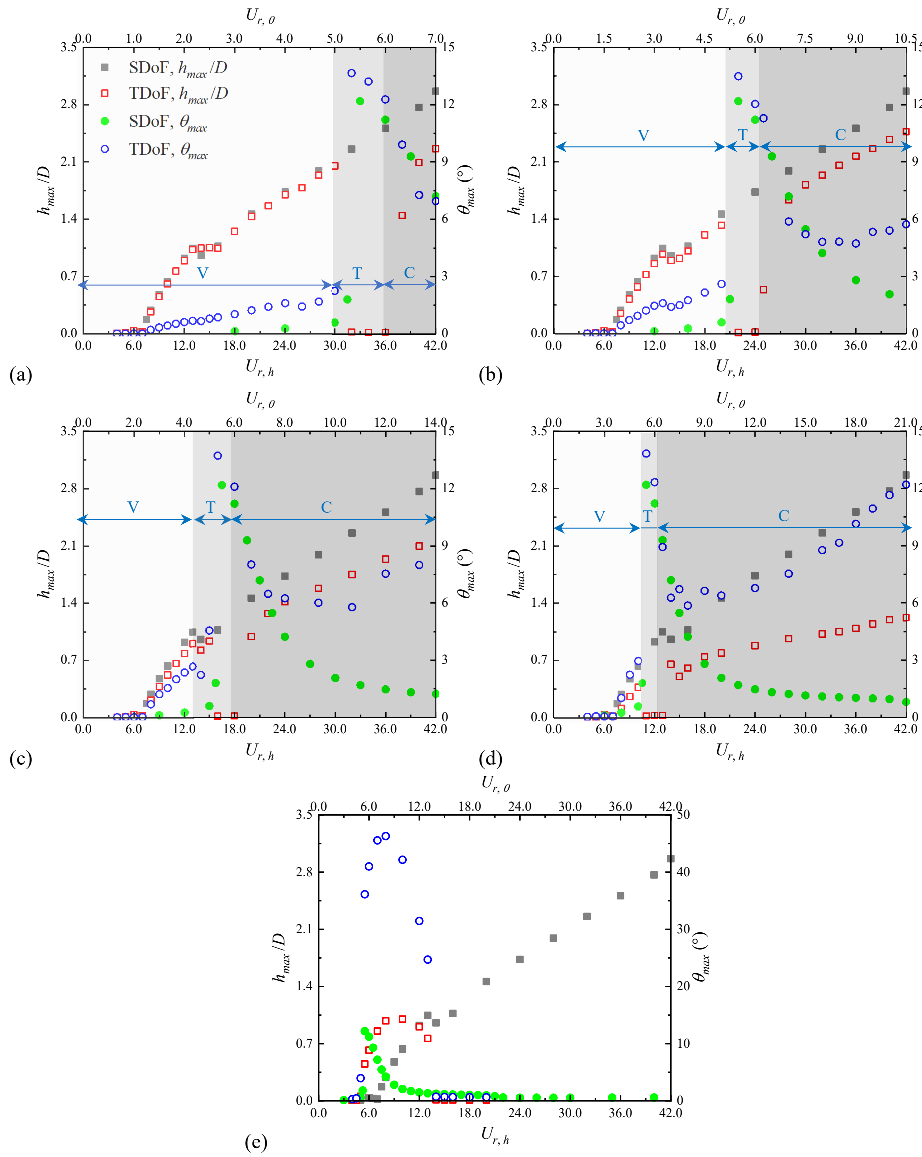

FIG. 3. Steady-state vertical and torsional vibration amplitudes of cylinder-plate assemblies with various frequency ratios: (a) $f_{\theta,0}/f_{h,0}$ = 6; (b) $f_{\theta,0}/f_{h,0}$ = 4; (c) $f_{\theta,0}/f_{h,0}$ = 3; (d) $f_{\theta,0}/f_{h,0}$ = 2; (e) $f_{\theta,0}/f_{h,0}$ = 1. The shading and arrows only apply for the TDoF cases.

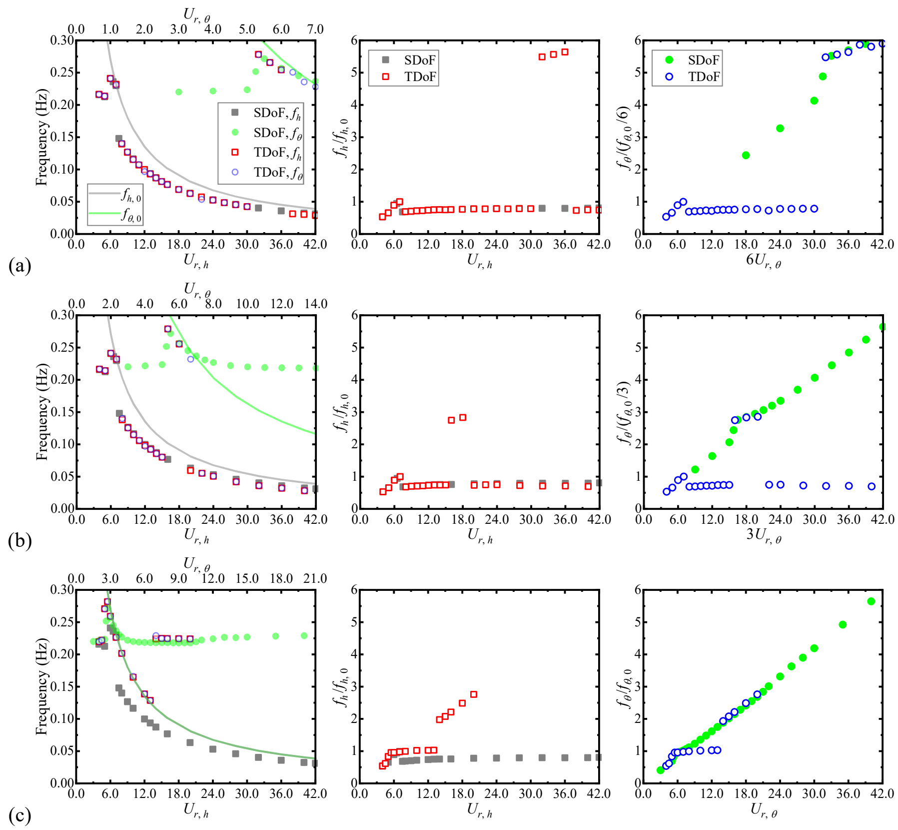

FIG. 4. Steady-state vertical and torsional vibration frequencies of cylinder-plate assemblies with various frequency ratios: (a) $f_{\theta,0}/f_{h,0} = 6$; (b) $f_{\theta,0}/f_{h,0} = 3$; (c) $f_{\theta,0}/f_{h,0} = 1$.

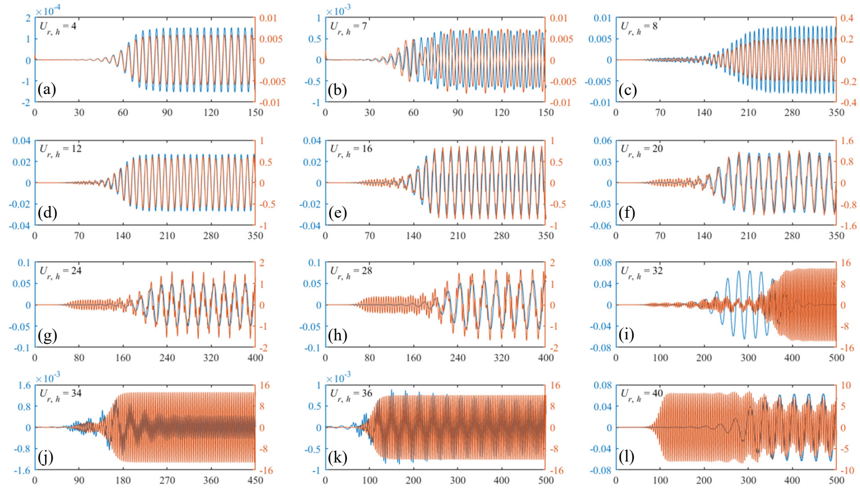

FIG. 5. Displacement signals of cylinder-plate assembly with $f_{\theta,0}/f_{h,0}$ = 6: (a) $U_{r,h}$ = 4; (b) $U_{r,h}$ = 7; (c) $U_{r,h}$ = 8; (d) $U_{r,h}$ = 12; (e) $U_{r,h}$ = 16; (f) $U_{r,h}$ = 20; (g) $U_{r,h}$ = 24; (h) $U_{r,h}$ = 28; (i) $U_{r,h}$ = 32; (j) $U_{r,h}$ = 34; (k) $U_{r,h}$ = 36; (l) $U_{r,h}$ = 40. The blue lines show dimensionless vertical displacements, while the red lines show torsional displacements. The horizontal axes are time in seconds. The left vertical axes are dimensionless vertical displacements, while the right vertical axes are torsional displacements in degrees (°).

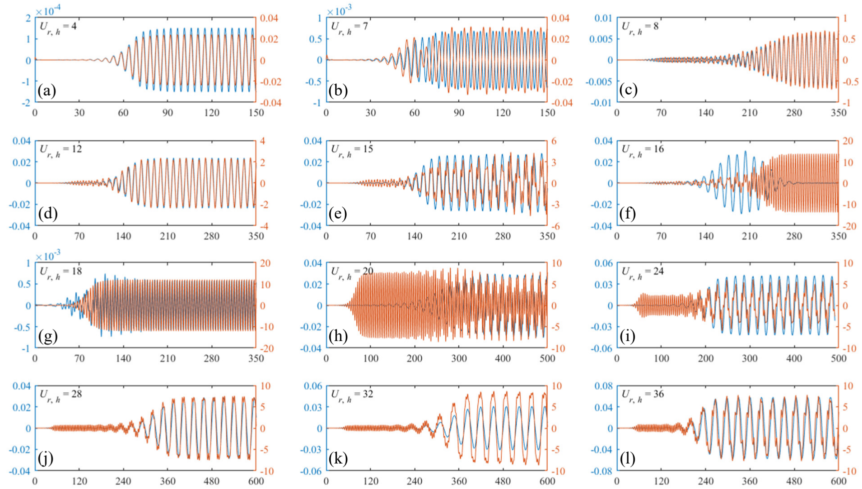

FIG. 6. Displacement signals of cylinder-plate assembly with $f_{\theta,0}/f_{h,0}$ = 3: (a) $U_{r,h}$ = 4; (b) $U_{r,h}$ = 7; (c) $U_{r,h}$ = 8; (d) $U_{r,h}$ = 12; (e) $U_{r,h}$ = 15; (f) $U_{r,h}$ = 16; (g) $U_{r,h}$ = 18; (h) $U_{r,h}$ = 20; (i) $U_{r,h}$ = 24; (j) $U_{r,h}$ = 28; (k) $U_{r,h}$ = 32; (l) $U_{r,h}$ = 36. The blue lines show dimensionless vertical displacements, while the red lines show torsional displacements. The horizontal axes are time in seconds. The left vertical axes are dimensionless vertical displacements, while the right vertical axes are torsional displacements in degrees (°).

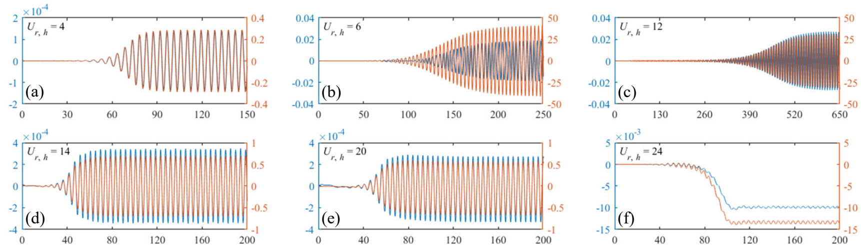

FIG. 7. Displacement signals of cylinder-plate assembly with $f_{\theta,0}/f_{h,0}$ = 1: (a) $U_{r,h}$ = 4; (b) $U_{r,h}$ = 6; (c) $U_{r,h}$ = 12; (d) $U_{r,h}$ = 14; (e) $U_{r,h}$ = 20; (f) $U_{r,h}$ = 24. The blue lines show dimensionless vertical displacements, while the red lines show torsional displacements. The horizontal axes are time in seconds. The left vertical axes are dimensionless vertical displacements, while the right vertical axes are torsional displacements in degrees (°).

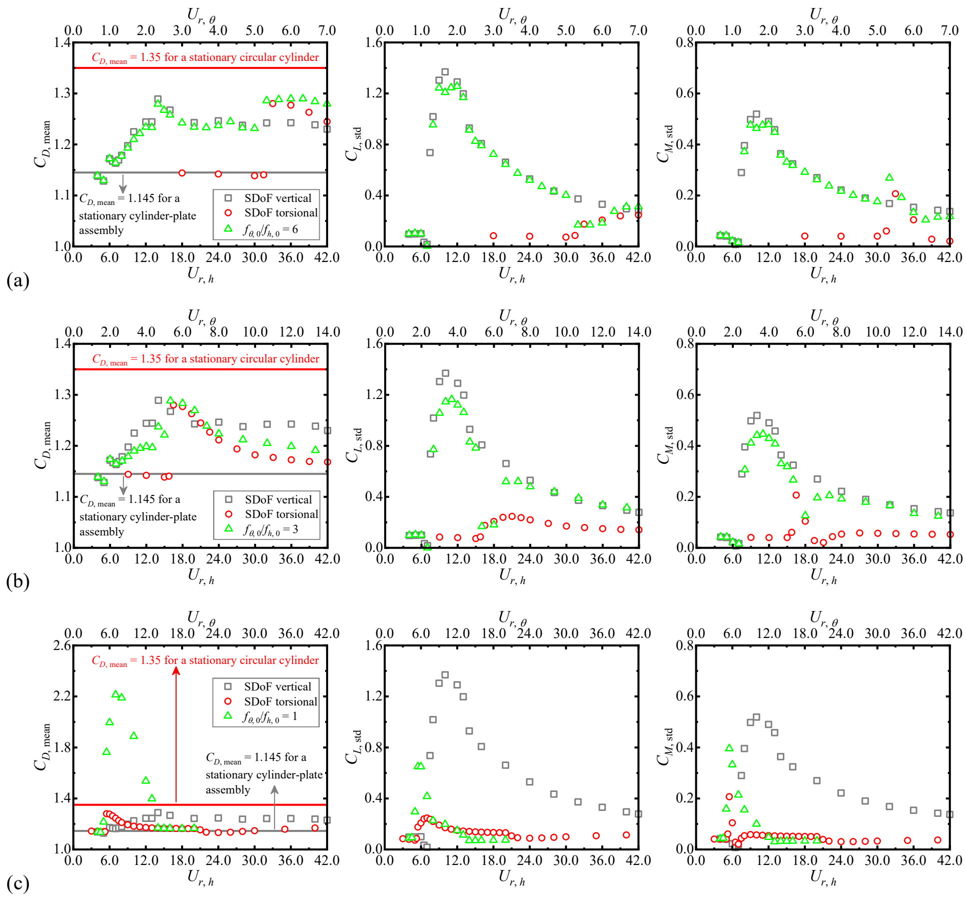

FIG. 8. Flow-induced force coefficients of cylinder-plate assemblies with various frequency ratios: (a) $f_{\theta,0}/f_{h,0}$ = 6; (b) $f_{\theta,0}/f_{h,0}$ = 3; (c) $f_{\theta,0}/f_{h,0}$ = 1.

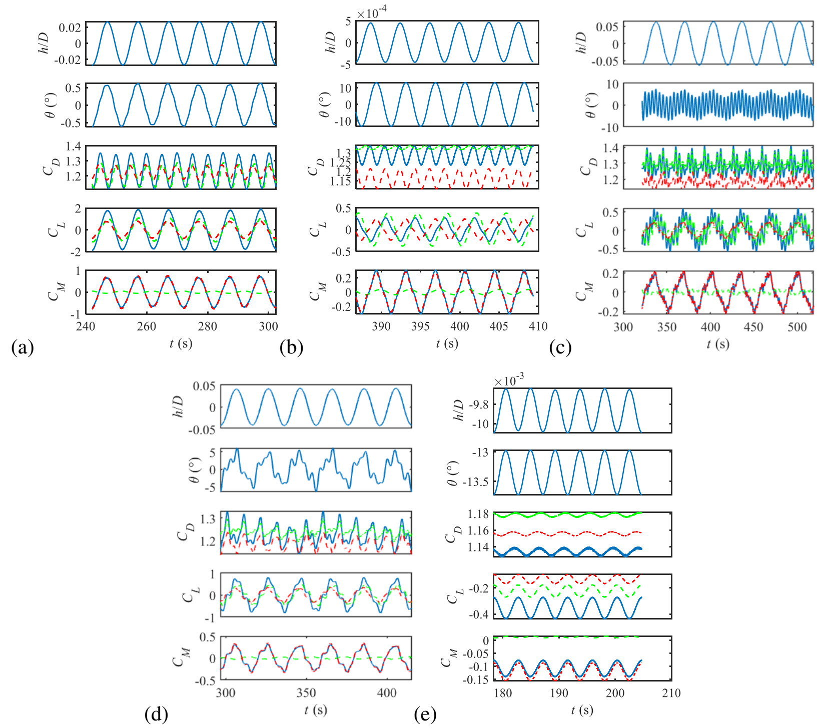

FIG. 9. Time histories of displacements and force coefficients of cylinder-plate assembly: (a) Case 1, $f_{\theta,0}/f_{h,0}$ = 6 and $U_{r,h}$ = 12; (b) Case 2, $f_{\theta,0}/f_{h,0}$ = 6 and $U_{r,h}$ = 34; (c) Case 3, $f_{\theta,0}/f_{h,0}$ = 6 and $U_{r,h}$ = 40; (d) Case 4, $f_{\theta,0}/f_{h,0}$ = 3 and $U_{r,h}$ = 24; (e) Case 5, $f_{\theta,0}/f_{h,0}$ = 1 and $U_{r,h}$ = 24. Solid blue line: displacement or force coefficient of cylinder-plate assembly; dashed green line: force coefficient of circular cylinder; dashed red line: force coefficient of splitter plater.

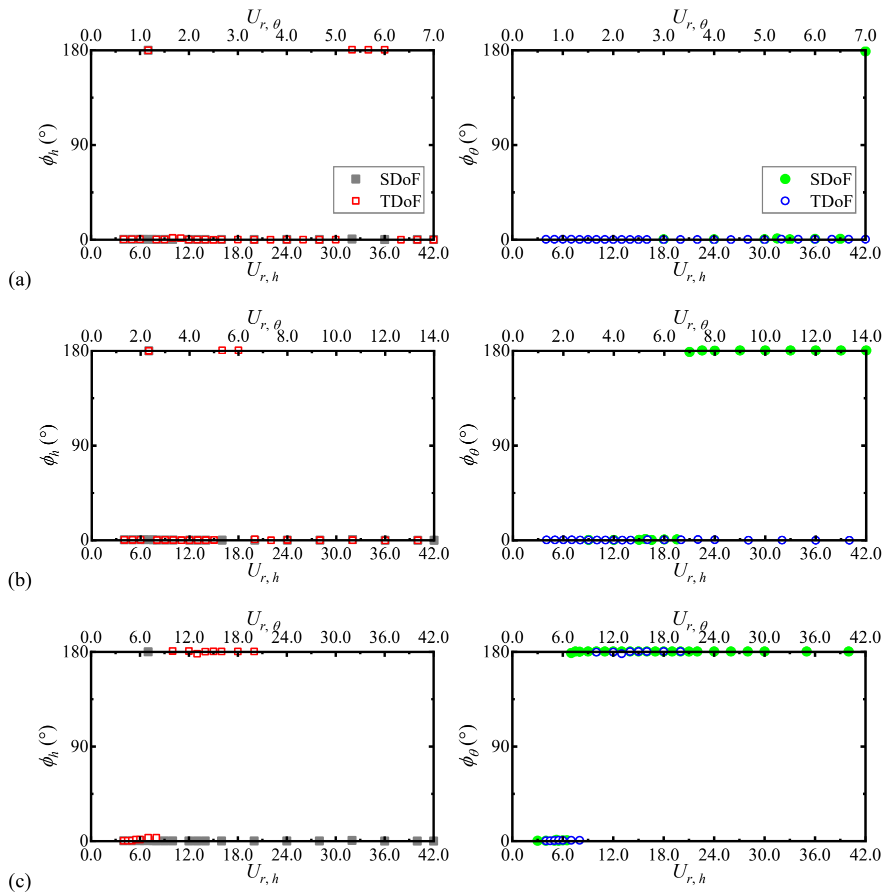

FIG. 10. Phase differences between lift force and vertical displacement, and between torsional moment and torsional displacement for circular-cylinder assemblies with various frequency ratios: (a) $f_{\theta,0}/f_{h,0}$ = 6; (b) $f_{\theta,0}/f_{h,0}$ = 3; (c) $f_{\theta,0}/f_{h,0}$ = 1.

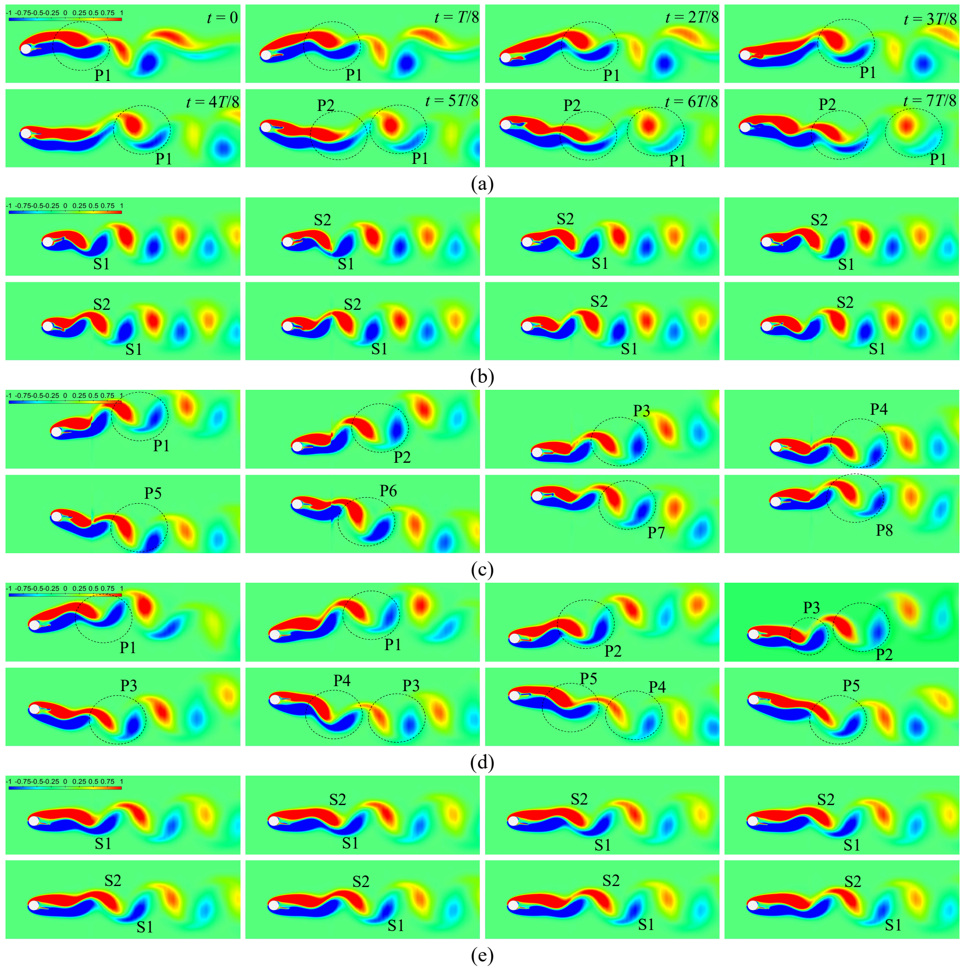

FIG. 11. Instantaneous vorticity fileds within one vibration cycle: (a) Case 1, $f_{\theta,0}/f_{h,0}$ = 6 and $U_{r,h}$ = 12; (b) Case 2, $f_{\theta,0}/f_{h,0}$ = 6 and $U_{r,h}$ = 34; (c) Case 3, $f_{\theta,0}/f_{h,0}$ = 6 and $U_{r,h}$ = 40; (d) Case 4, $f_{\theta,0}/f_{h,0}$ = 3 and $U_{r,h}$ = 24; (e) Case 5, $f_{\theta,0}/f_{h,0}$ = 1 and $U_{r,h}$ = 24.